Pascal Bliem, Oliver Beyß, Fatim-Zahra Mouhib

Computational and experimental investigation of the grain size dependency of the thermal expansion of Nb thin films

Supervisors:
Prof. Jochen M. Schneider, Ph. D.
Philipp Keuter, M. Sc.

Hauptseminar Report, Aachen, 30st August 2017

Abstract

Several studies reported a grain size-dependent thermal expansion in nano-crystalline materials, which is commonly attributed to the large amount of atoms located in grain boundaries (GBs). This effect can be of technological interest, since it may allow for tuning the thermal expansion coefficient. However, the reported magnitude of this effect varies strongly in literature and is most likely influenced by additional microstructural sample features, besides GBs.

In this work, we study grain size-dependent thermal expansion at the examples of Nb and Cu with different computational approaches, and create a foundation for an experimental investigation of this effect in Nb thin films. Molecular dynamics simulations of Cu systems with GB fractions ranging from 0 to 58.2% show an increase in the linear thermal expansion coefficient, α_L, of 8.7%. In contrast, Nb systems with GB fractions ranging from 0 to 67.5% show an overall decrease in α_L of 3.7%, while over a temperature range from 100 to 300 K, an increase in α_L of about 5% is still observed. Ab initio density functional theory simulations in conjunction with the Debye-Grüneisen model were used to calculate the thermal expansion of single-crystals, as well as disordered, under-coordinated and under-dense systems of Nb and Cu, created to resemble GBs. In a rule-of-mixture approach, α_L increases up to 18%, depending on GB density and GB fraction, which results from a reduction of Debye temperature with decreasing density. Nb systems with crystalline grains embedded in GBs reveal a 11.2% decrease in α_L with GB fraction increasing from 44.8 to 77.1% that emerges from larger Grüneisen parameters. This can be reasoned with the higher compressibility of the GB component within the employed model.

Nb thin films of about 1 μm thickness were deposited via DC magnetron sputtering with substrate bias varying from floating (-10 V) to -200 V. All samples consist of (110) textured bcc Nb with an O concentration of around 5 at%. A decrease in average grain size, based on Scherrer and Williamson-Hall equations, of about 40 to 32%, respectively, with increasing negative bias is observed. Accordingly, the Nb thin film samples are well suited for upcoming thermal expansion studies by wafer curvature method.

Contents

1.   Introduction

The thermal expansion coefficient is a highly relevant characteristic in engineering applications; particularly, if different materials are joined together, as in composites or coating-substrate systems. Mismatching expansion can be a source of large stresses in systems with different conjoined materials, potentially causing structural failure [1]. Hence, tunability of a material's thermal expansion coefficient may be of great technological interest.

Several studies [2–14] on nano-crystalline (NC) materials suggest that thermal expansion increases with decreasing grain size (D), which means, with an increasing fraction of grain boundaries (GBs). This phenomenon is attributed to the enhanced thermal displacement of atoms located in the GBs. Controlling grain size might, therefore, allow to tune thermal expansion. However, the reported magnitude of a D-dependency varies from almost zero [11] to more than hundred [5, 14] percent and thermal expansion seems also to be influenced by several factors (e.g. residual stresses, porosity, microstructural changes, chemical composition) that are often not fully considered in experiments.

In order to investigate various influencing parameters separately, atomic simulations can be of great aid, since they offer a high degree of insight and control, and can help to predict or explain physical effects. Using classical Newtonian molecular dynamics (MD) [15], one can create poly-crystalline systems and directly evaluate the change of volume with temperature. Yet, such simulations require accurate potentials, which are not available for numerous elements and most compounds. Ab initio electronic structure calculations [16], on the other hand, are flexible regarding the choice of compounds, but are computationally very demanding. Thus, the amount of atoms is usually limited to a few hundred, which makes it challenging to create representative systems. Furthermore, several approximations [17] have to be used to calculate thermal expansion from ground state properties. For these reasons, it is indispensable to validate such models with corresponding experiments. Bcc Nb is a well suited candidate for these investigations because its cubic crystal symmetry leads to an isotropic expansion and its high melting point allows for measurements over a large temperature range, without inducing significant grain growth. Fcc Cu is of interest as well, since some experimental data on D-dependent expansion is available in literature [5, 12].

Considering the mentioned aspects, the aim of this work is to study the potential grain

size-dependency of thermal expansion at the examples of Nb and Cu by using different computational approaches, as well as to set a foundation for an experimental investigation of this effect in Nb thin films. To fulfil this goal, we will present a comprehensive review covering properties of NC materials with a focus on grain size-dependent thermal expansion, as well as experimental methods for determination of thermal stresses and grain sizes in thin films. This will be followed by MD and ab initio simulations of Nb and Cu, and succeeded by chemical, structural, and diffraction peak broadening-based grain size characterisation of Nb thin films deposited by direct current magnetron sputtering (DC-MS), which will be shown to be suitable for intended thermal expansion measurements. Finally, an outlook on the experimental assessment of grain size-dependent thermal expansion will be given.

2. Review

2.1 Properties of nano-crystalline materials

Nano-crystalline or nano-structured (NS) materials are materials in which the microstructural building blocks, such as grains, are smaller than a micrometer. This includes components with reduced dimensions or mass such as nano-wires and thin films, as well as bulk and composite materials with nano-scaled microstructural features. A reduced grain size, D, results in a higher density of inter-granular defects such as grain boundaries (GBs), triple lines, and quadruple junctions. Grain boundaries can be separated in three categories [18, 19]: Low-angle dislocation boundaries, dislocation-free "special" high-angle low-energy GBs, and general high-angle GBs. The cores of first two categories of GBs are two-dimensional periodic arrangements of atoms that locally minimise the energy in the potential field of the adjacent crystallites. In contrast, general high-angle (and high-energy) GBs consist of completely overlapping dislocation cores in which the atomic disorder is distributed homogeneously, analogous to surfaces of amorphous materials. This type of GB is expected to be the most frequently present one in non-textured NC materials due to the numerous misorientations and boundary inclinations every grain is facing [19]. Furthermore, small grains can only accommodate little elastic strain, and thereby, only limited translations that

would increase the atomic density of the GBs. Various synthesis techniques, such as consolidation of inert gas condensed powders [20] and some physical vapour deposition methods [21] are known to incorporate large amounts of pores or voids, gas inclusions, and vacancies in the material, which further lowers its density. Gleiter [22] argues that, depending on the material, the GB density can be up to 15 to 30% lower than the crystalline density. However, other studies [23, 24] on NC Pd report that the GBs' structure does not differ significantly from the ones in the coarse-grained counterpart. Such apparent discrepancies suggest that the structural properties of a NC sample may depend strongly on the type of material and applied synthesis techniques.

The concentration of atoms in high-energy inter-granular defects in NC materials may have an effect on their properties. For example, it has been reported that thermal expansion and specific heat capacity are enhanced with an increasing fraction of atoms located in inter-granular defects [22]. These observation are generally explained by the assumption that in the less dense GB, atoms are under-coordinated and their bonds are elongated. This would cause the interatomic potential to be flatter and more anharmonic, resulting in a larger displacement from the equilibrium position with increasing temperature [22]. Table 2.1 contains a condensed overview of the reviewed studies, which will be examined in detail in the following. Here, the linear thermal expansion coefficient, α_L, will always be given in units of $\times 10^{-6}$ K^{-1}.

Fitzsimmons et al. [2] measured the thermal expansion parallel and normal to the interface plane for the large-angle twist GB in Au with synchrotron X-ray diffraction (XRD) and report that α_L along the direction normal to the interface plane at 255 K is found to be 3 times larger than α_L parallel to the interface plane and in the bulk. Wagner [3] tried to approximate properties of GB in NC materials by calculating them for a crystalline structure that is dilated to have a reduced density (or excess volume, ΔV) comparable to the GB. The results show that with increasing ΔV, the Debye temperature decreases and the Grüneisen parameter increases, which means the interatomic potential becomes more anharmonic. Accordingly thermal expansion and heat capacity increase with increasing ΔV. An exemplary calculation for Pd (D=9 nm) with a GB fraction of 30% and a GB ΔV of 30% results in an α_L increase of 70 to 85%. Zhu et al. [4] proposed a thermodynamic model, using experimental data as input, to predict D-dependence of melting point, Debye temperature,

3

Material	D(nm)	α_L(x10^{-6} K^{-1})	$\Delta\alpha_L$(%)	Method	T(K)	Ref.
Al, (thin film)	*	30.0-18.2	-40	cantilever bending	303-363	[14]
Cr, (thin film)	27-21	6.8-13.6	100	wafer curvature	298-623	[13]
CrN, (thin film)	13-7	6.7-10.6	58	wafer curvature	298-623	[13]
Cu, (gas condensed, consolidated)	c.g.-8	16.5-31.0	100			[5]
Cu, (thin film)	40-25	17.4-18.8	8	XRD	173-298	[12]
Ni, (electro-deposited)	10^5-20	10.0-10.1	1	dilatometry	140-500	[11]
Ni, (thin film)	50-35	12.6-13.7	9	XRD	173-298	[12]
Ni$_{80}$Pd$_{20}$, (crystallized, multi-phase)	127-8	15.5-20.7	34	thermo-mechanical	300-400	[8, 9]
Pd, (model)	c.g.-9	13.5-24.1	79	quasi-harmonic calculations	200-600	[3]
Pd, (gas condensed, consolidated)	c.g.-8	7.9-7.9	0	XRD	16-300	[7]
Se, (crystallized)	46-13	32.0-42.0	31	XRD	88-325	[10]
Ti, (thin film)	*	9.0-21.2	135	cantilever bending	303-363	[14]
Ti-Al-O-N, (thin film)	39-27	8.0-8.0	0	XRD	298-923	[25]

Table 2.1: *A condensed overview of the reviewed studies. The columns display the investigated material systems, the grain size range (c.g. stands for coarse-grained), the measured range of α_L and its relative change, the employed method, and the considered temperature range. * Grain sizes were not given in this reference. Instead the film thicknesses ranged from 1.7 to 0.3 μm for Al and from 0.3 to 0.1 μm for Ti.*

thermal expansion, and specific heat capacity. The predicted trends are essentially the same as in Wagner's work.

Experimental investigation on the D-dependence of α_L already started in the μm regime. Klam et al. [5] measured the expansion of a Cu foil (D=17 μm) mounted on a Cu block (D=19 mm) between 293 and 303 K. From the foil buckling they deduced that, depending on assumptions

of thickness and elastic properties of GB, the GB α_L should be 2.5 to 5 times higher than the bulk α_L. They also refer to studies in which consolidated gas condensed Cu ($D=8$ nm) had an α_L of 31, about a factor 2 larger than the coarse-grained α_L. Rupp et al. [6] measured an increased specific heat capacity in consolidated gas condensed Cu ($D=8$ nm) and Pd ($D=6$ nm) between 150 to 300 K. They attributed their observation to the weaker interatomic coupling of GB atoms and inferred that α_L should be increased, as well. In contrast to these studies, Eastman et al. [7] performed quantitative XRD measurements on Pd ($D=8$ nm) from 16 to 300 K and did not find any D-dependence of α_L. Instead, they found large static displacements of atoms from their equilibrium position due to tensile and compressive strains which originated from the consolidation process of nano-meter sized powders. They suggest and that previously reported changes in α_L might be due to effects resulting from manufacturing rather than from inherent features of NC materials. Turi et al. [11], supporting this argument, cite a conference presentation stating that the difference in α_L for NC Cu depends strongly on the consolidation pressure of inert gas condensed powder, decreasing with higher consolidation pressures. Other authors tried to synthesise fully dense NC samples with less intrinsic defects, besides GBs. Lu and Sui [8, 9] investigated thermal expansion over a temperature range from 300 to 400 K in Ni$_{80}$Pd$_{20}$ samples with D ranging from 8 to 127 nm, crystallised from melt-spun amorphous ribbons. With reduced D, α_L increased monotonically by about 34%, from 15.5$\pm$1.0 to 20.7$\pm$1.5. α_L of the polycrystalline ($D>10$ μm) and as-quenched amorphous alloy were 13.7 and 14.2, respectively. However, the crystallised samples consisted of two phases (fcc Ni and bct Ni$_3$Pd), which makes it impossible to judge how much of the difference in α_L resulted from a change in D and how much from a change in the phase fractions. Zhao et al. [10] crystallised porosity-free elemental hexagonal Se ($D=13$ to 46 nm) from amorphous Se. They measured the change in unit cell volume by XRD from 88 to 325 K. With decreasing D, it was observed that the unit cell expansion increased by about 31%, with an average α_L changing from 32 to 42. Besides the overall positive thermal expansion, the authors noted that their samples contracted along the c-axis. α_L of a coarse-grained reference was 26. Turi et al. [11] synthesised fully dense Ni ($D=20$ nm) by electro-deposition and compared it to Ni ($D=100$ μm) from 140 to 500 K. While the specific heat of NC Ni was 2.5 to 5% lager, α_L was only slightly larger at low

temperatures (7.8 vs. 7.2 at 140 K) and slightly lower at high temperatures (12.4 vs. 12.8 at 500 K). They concluded that the large differences in α_L reported in other publications are primarily due to porosity.

More recently, studies on a D-dependence of α_L have also been conducted on thin films. Kuru et al. [12] investigated 50 nm thick thin films of Ni (D=35 and 50 nm) and Cu (D=25 and 40 nm) from 173 to 298 K, deducing α_L from the change in the stress-free lattice parameter via XRD. They found α_L of Ni to be 13.7$\pm$0.4, 12.6$\pm$0.2 and 12.4 for D=35 nm, D=50 nm, and a coarse-grained reference, respectively. For Cu, α_L was 18.8$\pm$0.4, 17.4$\pm$0.4 and 15.7 for D=25 nm, D=40 nm, and a coarse-grained reference, respectively. This corresponds to an increase in α_L of about 2-10% for Ni and 11-20% for Cu, comparing the NC films to a coarse-grained reference. Daniel et al. [13] studied thermal expansion from 298 to 623 K in metallic Cr (D=21 to 27 nm) and ceramic CrN (D=7 to 13 nm) thin films. D was changed by varying the film thicknesses from 100 nm to 3 μm. The authors calculated α_L from measurements of thermal stress by wafer curvature measurement, while they tried to exclude the influence of residual stresses with the aid of XRD stress measurements. With the relatively small decreases in D, large increases in α_L were observed, from 6.8 to 13.6 (100%) for Cr, and from 6.7 to 10.6 (58%) for CrN. Fang et al. [14] were also measuring thermal expansion for thin films of different thickness from 303 to 363 K, using a bilayer (film on SiO_2) micro-cantilever curvature technique. For Ti films (0.1 to 0.3 μm thickness), exhibiting tensile residual stresses, α_L decreased with increasing thickness about 57%, from 21.2 to 9.0 (8.6 for coarse-grained bulk). The direction of this trend agrees with the observations of Daniel et al. For Al films (0.3 to 1.7 μm thickness), exhibiting compressive residual stresses, the trend was reversed: α_L increased with increasing thickness by about 64%, from 18.2 to 30.0 (23.1 for coarse-grained bulk). Holzapfel [25] measured thermal expansion with XRD from 298 to 923 K in arc-deposited Ti-Al-O-N films (D=27 to 39 nm, increasing with decreasing O content). He did not observe a change in α_L=8 as a function of D, O content, or residual stresses, and suggested that there might be TiO_2 sheet layers at the GBs which counteract an enhanced expansion.

The results from the studies reviewed above are rather inconclusive when it comes to determining the magnitude or even the existence of a D-dependent thermal expansion that can be

attributed only to the inherent nature of inter-granular defects. The expected anti-proportional relationship between D and thermal expansion varies over different length scales, sometimes zero or only a few percent, sometimes more than a hundred percent, and sometimes the trend is even reversed. Beside the increased fraction of atoms located in GBs, a couple of other factors seem to play important roles: Residual stresses and porosity, possibly changing with temperature, can effect the vibrational properties of materials such as thin films or high-pressure consolidated powders. In materials with anisotropic expansion, crystallographic texture can play a role if the expansion is measured macroscopically, e.g. with dilatometry. Compositional or microstructural changes, such as grain growth, can occur during heating and influence the measured results. Therefore, it is important to be aware of these influences and choose appropriate synthesis and characterisation techniques. Accordingly, the next sections will be dedicated to methods and their suitability for the characterisation of thermal expansion of thin films and the determination of the grain size.

2.2 Thermal expansion from wafer curvature measurement

Wafer curvature measurement is a common method for analysing stresses in thin films. The idea is to measure the curvature of film and substrate that occurs when the thin film is under tensile or compressive stress, to quantify the stress in the film. Figure 2.1 shows the development of the sample curvature for a film with a larger a) or smaller b) α_L than the substrate. When the sample is cooled from the deposition temperature, the film in scenario a) shrinks more than the substrate, which leads to tensile stress in the film and compressive stress in the substrate as the compatibility requirement needs to be fulfilled. However, the state in the middle picture does not represent mechanical equilibrium, because the torque at both ends needs to be compensated. Therefore, the sample is bent concavely upwards. In scenario b) the sample bends concavely downwards, respectively. To measure this curvature, a group of parallel lasers is aligned perpendicular or at a glancing angle to the film surface, and their reflection is to be observed. If the film is under tensile stress, the incidents of reflection move closer to each other and vice versa. From this, the radius of curvature of the sample can be obtained and inserted into the so-called Stoney equation. Thus, the
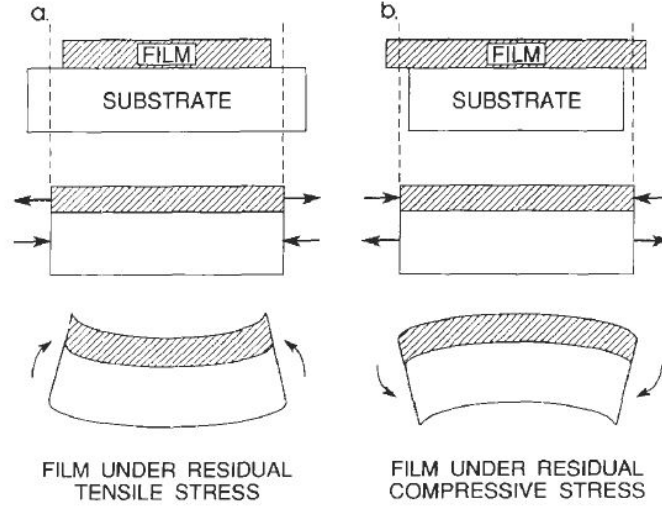
Figure 2.1: *Sample curvature under (a) tensile stress with $\alpha_L^f > \alpha_L^s$ and (b) compressive stress with $\alpha_L^f < \alpha_L^s$* [21].

stress can be approximated as [13, 21]

$$\sigma_f = \frac{1}{6}\frac{E_s}{1-\nu_s}\frac{d_s^2}{d_f}\frac{1}{R}. \tag{2.1}$$

In this equation, σ_f is the stress in the thin film, E_s, ν_s and d_s are the elastic modulus, Poisson's ratio and thickness of the substrate, respectively, d_f is the film thickness and R is the radius of curvature. Hereby, $d_s \gg d_f$ is assumed, which is usually the case for thin films. The expression $E_s/(1-\nu_s)$ is known as the biaxial modulus of the substrate and is often taken to be 180 GPa for Si (100) wafers in the literature [26, 27].

σ_f consists of an extrinsic stress component σ_{th}, mainly due to the mismatch of thermal expansion of film and substrate, and an intrinsic stress component, which may result, for example, from growth mechanisms or argon implantation. To obtain the linear coefficient of thermal expansion, α_L, of the film, only the thermal stress (i.e. the extrinsic stress) is of interest as it can be determined by [13, 21]

$$\sigma_{th} = \frac{E_f}{1-\nu_f}(\alpha_L^s - \alpha_L^f)(T - T_D), \tag{2.2}$$

where E_f, ν_f, α_L^f, α_L^s, T_D are the elastic modulus, Poisson's ratio and α_L of the film, α_L of the substrate and the deposition temperature, respectively. It is obvious that there is no thermal stress if $T = T_D$ or if α_L of film and substrate are equal. Based on this equation, α_L of the film can be calculated by considering the slope of the film stress over the temperature; thus, neglecting all

8

intrinsic stresses, which are assumed to be temperature independent [13]:

$$\alpha_L^f = \alpha_L^s - \frac{d\sigma_{th}/dT}{E_f/(1-\nu_f)}.$$ (2.3)

Hereby, α_L^s of Si (100) substrates is measured to be $2.6\text{x}10^{-6}$ K^{-1} [13]. Even though α_L is a function of temperature, an average value for the measuring range of the temperature can be obtained. According to Daniel et al. [13] this is acceptable, because the temperature dependence cannot be resolved with sufficient accuracy using this method. In addition, mechanical property measurements are necessary to gain information on the elastic properties of the thin film [13].

In general, wafer curvature measurement is a powerful method for the determination of α_L in thin films as it can be carried out in situ and, according to Zhao et al. [27], yields similar results as double crystal diffraction topography (DCDT), while not being limited to single crystalline substrates. However, the minimal measurable curvature is limited due to experimental errors, such as mechanical vibrations, electronic noise or asymmetry of the laser beam cross-section [27]. The roughness of the sample further reduces the method's accuracy, because it cannot distinguish surface curvature and lattice curvature [27]. Thus, the curvature of the wafer must be sufficiently large to obtain reasonable results. A solution for this problem was found by Mézin et al. [28] by cutting the sample into a bevel so that film and substrate are easily bent and thereby increasing the curvature. At elevated temperatures, plastic deformation of the substrate can also be a source of error, as it was observed for Si substrates at 600 °C by Sahringer et al. [26]. Moreover, the method assumes the curvature to be uniform throughout the sample, which in reality depends on the growing conditions of the film. Subsequently, the measurement can yield different results upon slight displacement of the lasers [27]. One needs to take note that the sample surface is homogeneously structured, because surface patterns can allow for a partial relaxation of the sample. On a larger scale, Hsieh et al. [29] used surface patterning by laser treatment to reduce residual stresses in thin films. Finally, interpreting the stress data, the material system itself needs to be considered as there are numerous reasons for stress build-up or relief. For example, Ouled-Khachroum et al.[30] found a strong correlation between stress build-up and a phase transition in Ge$_2$Sb$_2$Te$_5$ while Lei et al. [31] observed the formation of a stress relieving interlayer in Ti/TiN bilayer thin films. Further possible reasons are precipitations, oxidation of the thin film, impurities in the film, or recrystallisation at

elevated temperatures. Also, the assumption that intrinsic stresses are temperature independent needs to be questioned.

In view of the many assumptions and limitations of the method it seems difficult to obtain accurate values for the thermal stress. However, wafer curvature is well suited for the observation of trends, as needed to obtain α_L, because most sources of error are temperature independent or can be minimised by an appropriate choice of the measuring range.

2.3 Determination of the grain size

In order to analyse the effect of the grain size on the thermal expansion coefficient in nano-crystalline materials, an accurate method for the determination of the grain size in the specimens has to be found. Since the grain sizes in thin films are generally in the order of several nanometres, a well known option is the Scherrer method [32]. Its accuracy depends on several factors, which will be discussed in the following. Furthermore, its efficiency will be compared to the direct determination of the grain size by transmission electron microscopy (TEM).

The determination of the grain size out of diffraction peak patterns bases on imperfect scattering due to lattice distortion. The displacement of atoms from their equilibrium position is partially caused by distortion fields around lattice defects, such as grain boundaries, twin boundaries, dislocations or stacking faults [33]. Consequently, a large grain boundary fraction leads to an increase of the lattice distortion and a shortening of the length of coherently scattered X-rays and, thereby, broadens the diffraction peaks. Nevertheless, it has to be considered that other lattice defects may influence the peak breadth, leading to an uncertainty of the resulting grain size [33]. Especially in poly-crystals with a grain size smaller than 100 nm [34], a broadening of the diffracted beam during X-ray radiation is observed. Assuming that the observed effect is related to an increasing grain boundary fraction, the mean grain size can be quantified by the Scherrer equation. This leads to an estimation of the crystallite size by [32, 34]:

$$D = \frac{K\lambda}{bcos\theta},\qquad(2.4)$$

where λ is the wave length and θ the Bragg angle. The grain size, D, in the direction perpendicular

to the reflection plane [35], is defined as the cube root of the grain volume, assuming that the grains are equal in size and shape. If the shape or the size differ, the mean cube root or the cube root of the mean grain volume are used to define the grain size [34].

Originally, the peak breadth, b, was defined by Scherrer as FWHM, the measured width of the diffraction peak at half of its maximum intensity, disregarding the background [32]. A Second definition was introduced by Laue in 1936. He proposed the area under the peak divided by its maximum intensity. Hence, the peak breath is equal to the width of a rectangle with the same height and area as the diffraction peak [34, 36]. In contrary to FWHM, the definition of Laue has a direct physical interpretation. It represents the volume average of the thickness of the grain perpendicular to the reflection plane [34]. Therefore, the corresponding Scherrer constant has been investigated more frequently [34, 36, 37]. Nevertheless, both methods can be equally accurate if the Scherrer constant is chosen carefully. The Scherrer constant, K, is a dimensionless parameter used to obtain a better approximation of the grain size. It takes several undesired influences on the peak broadening into account, such as deviations in shape or size, which lead to a decreasing accuracy. Consequently, K has to be chosen carefully to obtain a correct grain size [34]. Furthermore, the Scherrer constant has to be assimilated to the chosen definition of peak breadth. Although the determination of a specimen specific Scherrer constant increases the accuracy of the average grain size, the resulting value remains an estimation, since multiple influences on the peak breadth lead to a large error [34, 38]: Those are the grain size distribution, orientation, grain shape, instrumental broadening effects and residual stress. Minor changes in these factors can exert a major influence on the resulting grain size, since both, the peak breadth and the Scherrer constant, are highly sensitive to deviations in the factors stated above [34, 37]. It has to be noted that the Scherrer constant influences the result proportionally and can vary between approximately 0.8 and 1.5 [34].

Due to the research aim of this study, the exact grain size values are of minor interest, but rather a valid size trend of the samples to evaluate the size effect on the thermal expansion coefficient is needed. It can be assumed that the deviation of shape and size within a sample are negligibly small, provided that the experimental conditions in the coating chamber are uniform. Consequently, nearly non of the factors above are to be regarded as critical since they may influence the resulting grain

size value, but the final trend of the samples relative to each other remains the same. Accordingly, the critical influencing factor is the intrinsic stress in the samples. It emerges inevitably in thin films as a consequence of the deposition process. For example, a higher bias voltage leads to an increase of residual stress in thin films with small grain sizes [39, 40]. Consequently, the different bias voltages used in the deposition process (see Section 3.2) for the sample films cause a variation in peak broadening that has an impact on the resulting trend of the mean grain sizes [39, 41, 42]. Macro-strain is defined as a homogeneous expansion of the lattice parameter due to a change in the overall pressure it has no impact on the peak breadth, but rather shifts the peak position. Accordingly, it is of minor interest to the determination of the grain size[43], whereas micro-strain remains a critical factor.

A simple method to isolate the peak broadening due to micro-strain, ϵ_s, from the size effect was proposed by Williamson and Hall in 1953 [44, 45], stating that the peak broadening due to micro-strain depends on $\tan\theta$, where θ is the Bragg angle. Consequently, the overall broadening is described as:

$$b_{tot} = b_{Scherrer} + b_{\epsilon_s} = \frac{K\lambda}{Dcos\theta} + 4\epsilon_s \tan\theta. \tag{2.5}$$

So that,

$$b_{tot}\cos\theta = \frac{K\lambda}{D} + 4\epsilon_s \sin\theta, \tag{2.6}$$

Equation 2.6, permits the calculation of the micro-strain, ϵ_s, based on the slope of the Williamson-Hall plot ($b_{tot}\cos\theta$ vs. $\sin\theta$). Additionally, an overall root mean square grain size can be gained out of the intercept. The given equation is valid for the assumption that both broadening effects can be described by a Cauchy approximation for the peak shape [38, 45]. Originally, the equation was derived for powder specimens and bases on several assumptions. The specimens have to be isotropic without a texture and the strain is expected to be uniform. Consequently, it has to be noted that the equation might be unfit for the usage in thin films, since the strain profile is mostly anisotropic and the microstructure consists of columnar grains with a preferred orientation [33]. Assuming the strain to be sufficiently small, the sample stress can be

calculated by applying Hooks law, as followed:

$$\sigma_s = \frac{E}{1 - v^2} \epsilon_s.$$ (2.7)

An alternative method for the determination of grain sizes is TEM, it is a direct visual method and has the advantage that it does not depend on assumptions regarding the given sample structure. On the other hand TEM measurements lack statistical efficiency, since it usually takes only a limited number of grains into account. This can be especially problematic in inhomogeneous samples. Furthermore the reliability of the results can suffer from particle overlap and contrast problems emerging during the detection of the particle boundaries. This notably affects small particles. A major advantage of XRD grain size analysis is a good statistical value and the simplicity of the Scherrer method for nano-crystalline materials. XRD measurements have a higher time efficiency and can, therefore, be preferable to the more precise TEM measurement. It has to be considered that both methods result in a different grain size. This is especially important while dealing with non-uniform grain shapes. While the Scherrer equation measures the cube root of the volume average of the grains, based on the direction perpendicular to the reflection plane [35], the TEM measurement visualizes the grain size parallel to the surface plane. However, both methods represent different approaches and the best choice depends on case specific requirements for accuracy and time efficiency [38, 46].

3. Methods

3.1 Computational details

Molecular dynamics (MD) simulations were performed with the large-scale atomic/molecular massively parallel simulator (LAMMPS) code [47]. The atomic interactions of Nb and Cu were described by embedded atom method (EAM) potentials developed by Fellinger et al. [48] and Mishin et al. [49], respectively. Poly-crystals with randomly oriented grains were produced by a Voronoi construction as implemented in the Atomsk code [50]. Cubic simulation cells had an initial side length of 150 Å, which resulted in about 160000 and 280000 atoms for Nb and Cu, respectively. The grain size was varied by the number of Voronoi nodes. Single-crystalline

simulation boxes had initial side lengths of 100 Å (87808 atoms) for Cu, and 100 Å (54000 atoms) and 200 Å (432000 atoms) for Nb. Periodic boundary conditions were used. The systems studied by classical MD (discussed in Section 4.1) are named by the chemical symbol, followed by -pc for poly-crystalline or -sc for single-crystalline and a number corresponding to the average grain size (for -pc) or cell side length (for -sc) in Å (e.g. Nb-pc13, Cu-sc100). Prior to MD simulations, atoms overlapping within a radius less than the nearest neighbour distance were removed, and the systems were relaxed by a conjugate-gradient algorithm. Subsequently, the systems were equilibrated towards 100 K and 0 pressure in an isothermal-isobaric (NPT, Nosé-Hoover thermostat and barostat as implemented in LAMMPS) ensemble with a time step of 0.2 fs until temperature, pressure, and volume remained constant. During subsequent heating (discussed in Section 4.1), thermodynamic data was output every 100 fs, averaged over the previous 100 fs. The open visualisation tool (OVITO) [51] was used for visualisation and parts of the post-processing: Crystal structures were determined by an adaptive-cutoff common neighbour analysis (CNA) [52]. It is known that the CNA algorithm can fail to identify atoms in a lattice due to large thermal displacements; therefore, the single-crystalline systems were used as a standard to correct GB fractions in poly-crystalline systems. Atomic volumes were calculated by a Voronoi tessellation with the atoms as nodes, and porosity was analysed by a surface mesh construction using the respective lattice parameter as probing sphere radius.

Electronic structure calculations were performed within the framework of density functional theory (DFT). An introduction to DFT can be found in Appendix section A.3. The systems investigated by DFT, which will be discussed in more detail in Section 4.2, were of three types: Single-crystals named by chemical symbol and structure (e.g. Nb-bcc); disordered, under-dense structures intended to resemble GBs, named by symbol, -gb, and density in g/cm^3 (e.g. Nb-gb6.3); and embedded grains surrounded by GB, named by symbol, -eg, and grain diameter in Å (e.g. Nb-eg10). Some of the disordered, under-dense structures in this study (Nb-gb6.3, Nb-gb5.0, Nb-gb4.1, Nb-gb3.5, Nb+O-gb4.6) were produced by a vapour-quench method using the Open-source Package for Materials Explorer (OpenMX) [53]. Systems were vaporised with a velocity rescaling thermostat for at least 1 ps with a time step of 1 fs and then quenched to 0 K.

The dynamic calculations utilized the PBE-GGA [54] exchange correlation functional, fully relativistic pseudo-potentials with partial core corrections, linearly combined localized pseudo-atomic orbitals as basis functions, a real space grid cutoff of 150 Ry, an electronic convergence criterion of 10^{-4} Hartree, and Brillouin zone integration at the Γ-point. The basis functions were chosen to be Nb7.0-s3p2d2 and O5.0-s1p1, where the chemical symbol is followed by the radial cutoff (in Bohr radii) and the used atomic orbitals. Some other systems (Nb-gb8.2, all Cu-gb, all Nb-eg) were produced, also by a vapour-quench method, in a canonical ensemble with a time step of 1 fs in LAMMPS, followed by a structural relaxation. For the embedded grain systems, the atoms belonging to the grain were fixed and only the surrounding GB atoms were annealed, quenched, and relaxed. The generated systems were used as an input for calculations at 0 K, performed by the Vienna ab initio simulation package (VASP) [55]. These calculations employed projector-augmented wave potentials within PBE-GGA, for which the projector functions were evaluated in real space if the system contained more than 50 atoms. First order Methfessel-Paxton smearing [56] was applied and the electronic convergence criterion was set to 10^{-4} eV. Prior to any static calculations, every system was structurally relaxed by a conjugate-gradient algorithm with a force convergence criterion of 10^{-2} eV/Å. During relaxation of the embedded grain systems, the atoms belonging to the grain were fixed, based on the equilibrium spacing of the single-crystalline counterpart. The equilibrium volume for all simulation cells was found by an Birch-Murnaghan equation of state [57, 58] fit. Basis set cutoffs were set to the maximum value recommended for the respective potential during relaxation and were further increased by 30% for static calculations. Brillouin zone integration was performed on Monkhorst-Pack [59] or Γ-point k-point grids, converged to ≤ 0.007 eV per atom. An insufficiently dense k-point mesh would usually result in a poor fit when determining elastic constants. This was not the case for any of the considered systems, which indicates that k-point meshes were sufficiently dense for our purpose. In all calculations, periodic boundary conditions were used.

Thermal expansion from ab initio calculations was calculated within the framework of the quasi-harmonic Debye-Grüneisen theory, which provides the possibility to calculate a system's free energy as a function of temperature and volume. Both the Slater [60] and Dugdale-MacDonald

(DM) [61] approximations for the Grüneisen parameter, γ, were used. The procedure of the Debye-Grüneisen model is described in detail in Appendix section A.1.

3.2   Experimental details

Nb thin films were deposited by direct current (DC) magnetron sputtering in an Ar atmosphere at 300 °C substrate temperature. The pressure during deposition was set to 5×10^{-3} mbar, while the base pressure was below 4×10^{-7} mbar. The target to substrate distance was kept constant at 10 cm. Sputtering was conducted with 150 W power supplied to the 2"-elemental Nb target (99.95% purity) while the substrate bias was varied from floating potential to -200 V in 50 V steps. The duration of the depositions was one hour leading to a film thickness of about 1 μm, which was determined indirectly by the measured mass gain assuming bulk density as well as directly by cross-section scanning electron microscopy (SEM) analysis. 2"-Si (100) wafers were used as substrates. After deposition the samples were vacuum sealed to avoid oxidation of the film.

Chemical analysis was performed via energy dispersive X-ray spectroscopy (EDX). Using an EDAX Genesis 2000 analyser mounted on a Jeol JSM-6480 scanning electron microscope. The samples were analysed with an acceleration voltage of 5 kV and a magnification of 1000x by maintaining a working distance of 10 mm. Data was collected during 60 live seconds. For each sample five measurements were carried out.

The average grain size was determined via X-ray diffraction (XRD). A Siemens D5000 diffractometer with a monochromatic Cu_{K_α} X-ray source was used (λ=1.5405 Å). The diffraction pattern was measured using unlocked-coupled scans in Bragg-Brentano geometry with a 2 ° offset within the 2θ angle range 10 to 90 ° with a step size of 0.05 ° and 3 s accumulation time per angular step. The grain sizes were calculated by means of the Scherrer equation applying a Scherrer constant K of 0.9.

4. Results and discussion
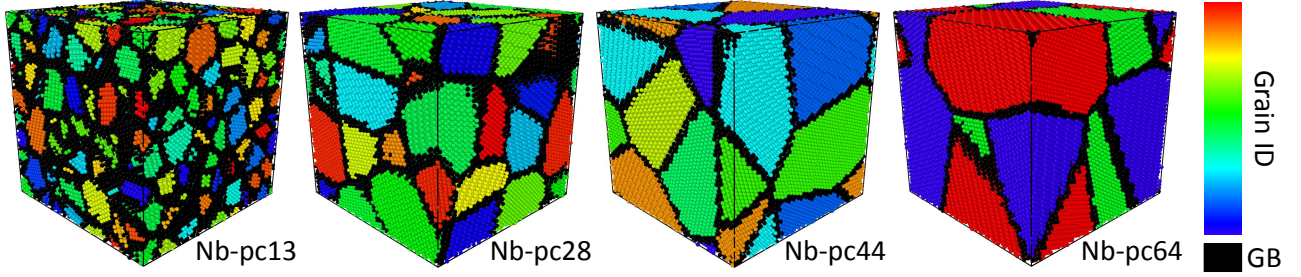
4.1 Heating by molecular dynamics

Figure 4.1: *Simulation cells of poly-crystalline Nb with varying grain size before relaxation. Every grain is coloured individually (Grain ID) and the GBs are coloured in black.*

To study D-dependent expansion of Nb and Cu via classical MD, systems with varying grain sizes were created and heated. Different poly-crystalline configurations are exemplarily shown for Nb in Figure 4.1. In addition, an overview of all systems studied by MD and their average grain size is given in Table 4.1. Table 4.1 also shows the corresponding fractions of atoms assigned to be part of a GB (identified by the CNA algorithm to not match a common lattice type), before relaxation, %GB$_{ini}$, after relaxation at 100 K, %GB$_{rel}$, and at the end of the whole heating process, %GB$_{fin}$. This quantity increases during relaxation, indicating that, in equilibrium, more atoms in the vicinity

System	D(Å)	%GB$_{ini}$	%GB$_{rel}$	%GB$_{fin}$	α_L(×10^{-6} K^{-1})	α_L^{corr}(×10^{-6} K^{-1})
Nb-pc13	12.8±2.1	58.9	67.5	57.6	7.05	9.13
Nb-pc28	28.2±3.0	31.9	35.6	39.5	8.75	9.40
Nb-pc44	44.2±3.8	21.9	24.0	27.4	8.93	9.35
Nb-pc64	63.9±3.8	15.5	13.8	16.7	9.29	9.42
Nb-sc100		0.0	0.0	0.0	9.51	9.45
Nb-sc200		0.0	0.0	0.0	9.52	9.47
Cu-pc13	12.8±1.9	49.2	58.2	62.8	16.51	18.43
Cu-pc28	28.0±4.4	25.8	29.9	36.7	17.52	18.10
Cu-pc44	44.0±5.1	16.6	18.9	23.7	17.45	17.65
Cu-pc62	62.0±1.6	12.5	12.8	15.9	17.27	17.42
Cu-sc100		0.0	0.0	0.0	16.98	16.96

Table 4.1: *An overview of all systems investigated by classical MD. The columns display the initial (before relaxation) average grain size, D, the initial fraction of atoms in GBs, %GB$_{ini}$, the fraction of atoms in GBs after relaxation at 100 K, %GB$_{rel}$, the corrected fraction of atoms in GBs at the highest temperature step, %GB$_{fin}$, and the uncorrected, α_L, and corrected, α_L^{corr}, averaged linear thermal expansion coefficients.*

of GBs are displaced from their ideal lattice position. For all systems except Nb-pc13, this value increases even further with heating, suggesting that atoms in proximity to GBs are subject to larger thermal displacements, compared to atoms in an ideal lattice.

In order to determine expansion with temperature, T, the systems were held at a constant T for 10 ps and then ramped to the next temperature for 10 ps. Figure 4.2 displays how the systems' volume changes over the duration of the simulation. Based on the averaged volumes, V, of the isothermal sections, α_L (always given in units of x10^{-6} K^{-1}) was calculated as $\alpha_L = \Delta V/(3V_0\Delta T)$, from one isothermal section to the next (see Table 4.1). The maximum T (700 K for Cu, 1300 K for Nb) was chosen not to exceed a homologous temperature of 0.5. Anyhow, some of the graphs indicated by the decreasing slope at constant T in Figure 4.2, corresponding to the systems with smaller grain sizes, exhibit an isothermal volume reduction. The CNA analyses show that this densification is not directly due to grain growth (cf. Table 4.1), but considering the short time scale, it might be an incubation period prior to grain growth. The high driving force resulting from high defect concentrations in small-grained systems and the thermal energy allow atoms to reorient into denser configurations. This effect is bothersome if α_L should only be attributed to expansion stemming from atoms' thermal oscillations around fixed relative positions; therefore, we attempted
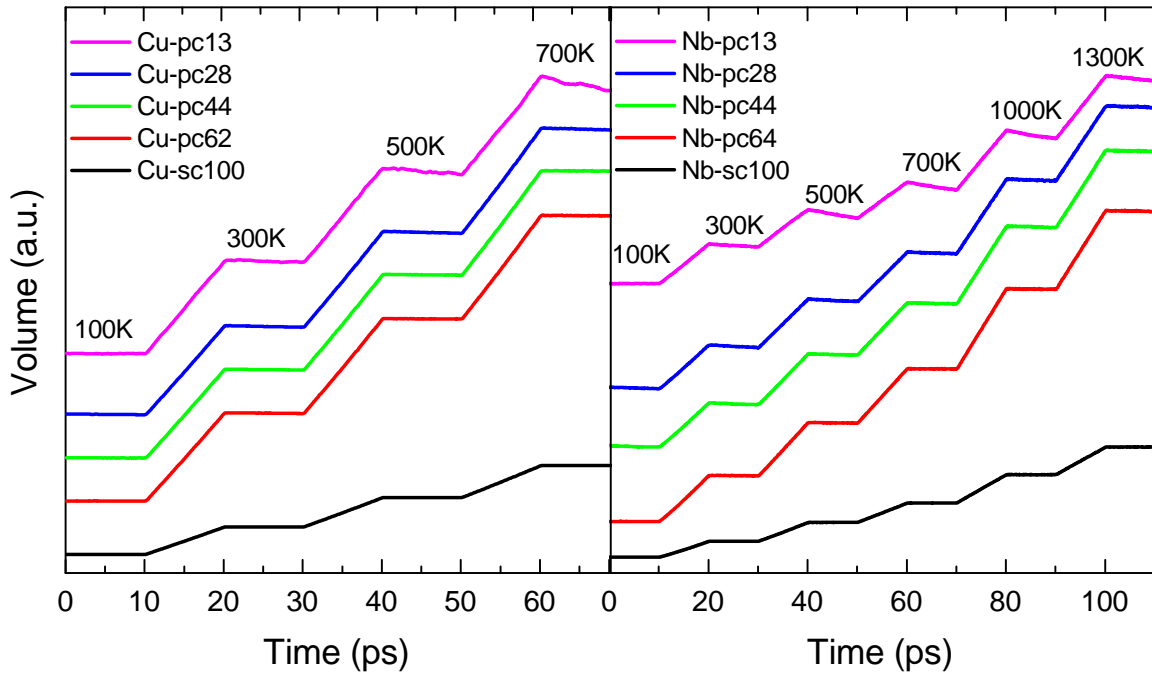

Figure 4.2: *Change of volume with simulation time for all systems. Isothermal sections are indicated by the respective temperatures. The graphs are offset for clarity.*

to correct for the densification rates. They were obtained as the slopes of linear fits of isothermal sections and by interpolation with linear radial basis functions (as implemented in the SciPy [62] Python library) of non-isothermal sections.

The corrected linear thermal expansion coefficient, α_L^{corr}, as a function of GB fraction, %GB, is plotted in Figure 4.3 for the individual temperature ranges and averaged. Both averaged α_L and α_L^{corr} are also documented in Table 4.1. For Cu, expansion increases with increasing T. The value of $\alpha_L^{corr} \approx 16.5$ around 300 K for Cu-sc100 (%GB=0) agrees excellently with experimental data [63]. In addition, α_L^{corr} increases monotonically with an increasing fraction of atoms located in GBs. The difference in average α_L^{corr} between the single-crystal and the poly-crystal with the highest %GB=58.2 is 8.7%, which is representative for the individual temperature ranges. This increase is rather small, compared to values from 20 [12] up to 100% [5] reported in literature (cf. Section 2.1). Comparing the density of the GBs with that of the grains yields a difference of about 4% (e.g. for Cu-pc44: 12.3±0.6 vs. 11.7±0.2 Å^3/atom), which does not approach the 15 to 30% reported previously [22]. If the processing route in other studies resulted in GBs with significantly lower density, possibly containing pores, this might contribute to the high changes in
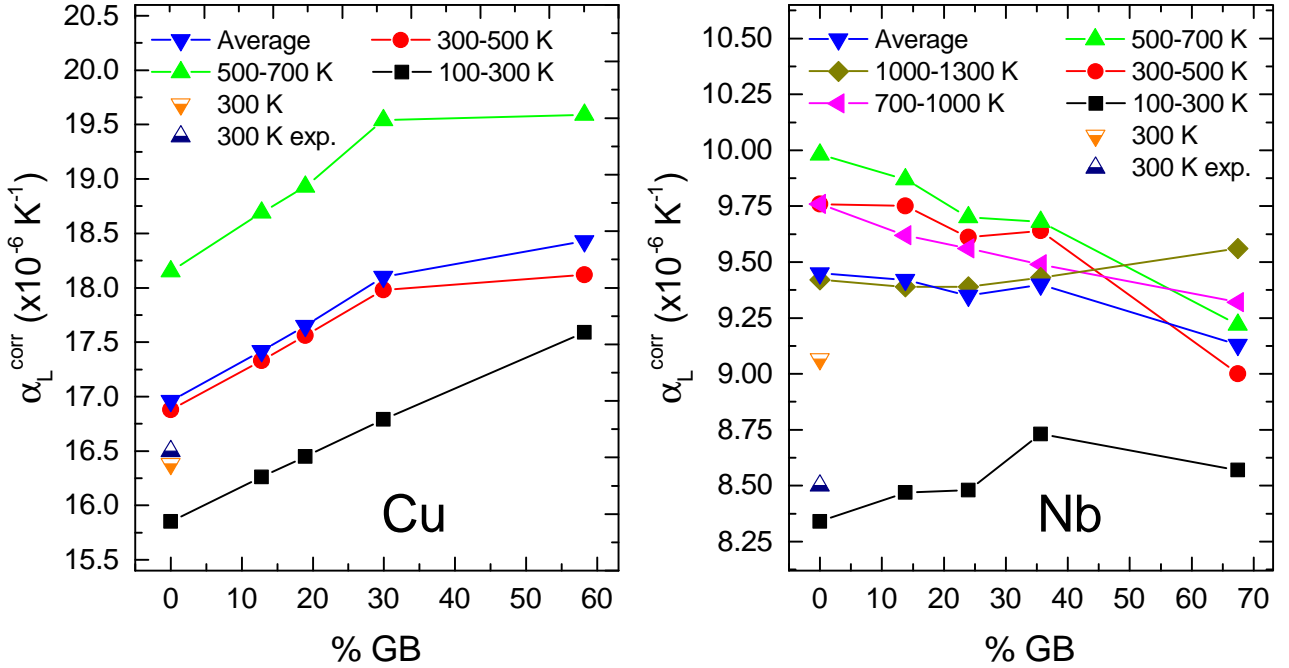

Figure 4.3: *Change of α_L^{corr} with %GB over different temperature ranges and averaged, as well as at 300 K (average of the 100-300 and 300-500 K ranges) and experimental data [48, 63] at 300 K for Cu (left) and Nb (right) systems.*

α_L reported. Mishin et al. [49] tested their EAM potential for Cu extensively, examining elastic properties, thermal expansion, and phonon dispersion, which were all in very good agreement with experiment. Consequently, the low change in α_L^{corr} is not an artefact of the potential, but can be considered as representative for systems similar to the ones investigated here.

The value of $\alpha_L^{corr} \approx 9.1$ around 300 K for Nb-sc100 (%GB=0) is higher than the experimental data ($\alpha_L \approx 8.5$) that Fellinger et al. [48] used to test their Nb EAM potential, which is in line with their observations. Beside this offset, the change of α_L with T agrees well with experiments in their test. A noteworthy system size-dependence (cf. Nb-sc100 vs. Nb-sc200 in Table 4.1) of α_L^{corr} was not detected. The average difference in α_L^{corr} between the Nb single-crystal and the poly-crystal with the highest %GB=67.5 is -3.4%. A decrease in α_L with increasing %GB, was rarely reported before [14]. For the lowest T range of 100 to 300 K, α_L^{corr} is increasing by about 5% with increasing %GB, except for the last data point (Nb-pc13, %GB=67.5). Since Nb-pc13 exhibits the most prominent densification of all systems and even grain growth (cf. Table 4.1), the correction scheme might not be able to fully deconvolve the effects of densification and expansion, and thus, not result in a monotonic trend. Over a T range from 300 to 1000 K, α_L^{corr} decreases with increasing %GB, which seems counterintuitive based on arguments reviewed in Section 2.1. This might be an artefact originating from the potential. Fellinger et al. [48] compared the phonon dispersion for their potential with experimental data and found that it agrees well with experiment at low wave vectors, but cannot correctly reproduce all features at the high wave vector Brillouin zone boundaries. The Debye temperature of Nb, at which all phonon modes are occupied, is Θ_D=275 K (based on our ab initio calculations). This means that in the range from 100 to 300 K mostly lower wave vector phonons are present, which are described well by the potential. Above Θ_D, the density of high wave vector phonons increases, which are not described properly by the potential. Scattering of such phonons at GBs might, hence, be described incorrectly in a way that causes the GB atoms to show a smaller thermal displacement than the grain atoms. However, the overall impact of the increased number of atoms located in GBs is rather small for Nb. The density of GBs is about 2.5% lower than that of the grains (e.g. for Nb-pc44: 18.7±1.0 vs. 18.2±0.3 Å³/atom). This is low in comparison to previous reports [22], similar to the Cu systems.

Generally, the observed differences in thermal expansion as a function of %GB, up to 8.7%, are small compared to some reported experiments, even though %GB was varied over a wide range, from 0 up to 67.5%. This might be partially due to the limited accuracy of the potential in case of Nb, but probably also because the samples in other studies had fundamentally different microstructures, marked by other defects, such as pores, inclusions, and residual stresses.

4.2 Ab initio calculations and Debye-Grüneisen model

DFT calculations can predict material properties very accurately, but due to their high computational demand, these simulations are limited to a few hundred atoms. Therefore, one cannot simply create a poly-crystal as in classical MD and different grain sizes (or rather GB fractions) have to be modelled indirectly. In a first approach, the GB component is modelled separately. Based on GB characteristics reviewed in Section 2.1, we created disordered, under-dense and under-coordinated structures (labelled with -gb) of different densities, ρ, intended to resemble GBs. In a second approach, crystalline grains of different size were embedded in such structures to represent poly-crystals over the periodic boundary conditions (labelled with -eg). Examples for the different approaches are depicted for Nb in Figure 4.4. An overview of the systems investigated by DFT is shown in Table 4.2.

For the -gb structures (see Figure 4.4 a)), ρ was lowered by expanding the cell size. Both Nb and Cu systems display a tendency to rather reduce their average atomic coordination, n, instead of stretching the average nearest neighbour bond length, l_B, which resulted in significant pore formation (see Table 4.2). With increasing porosity, ϕ, l_B even decreases slightly further, which can
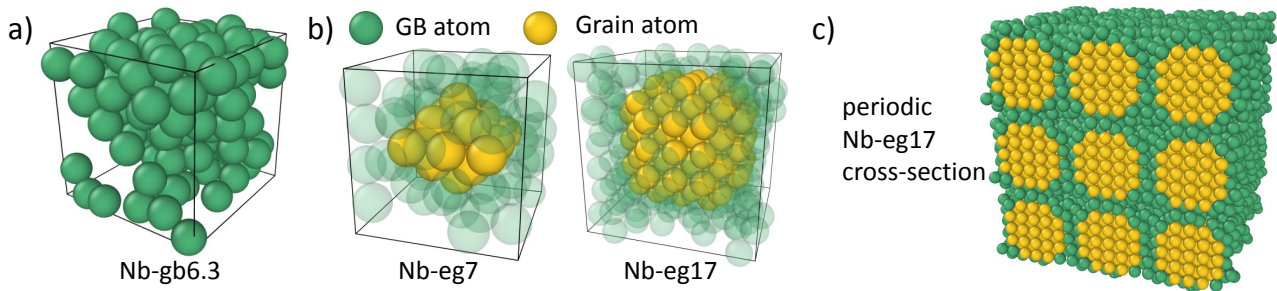

Figure 4.4: *a) Representative simulation cell of a -gb structure. b) Representative simulation cells of -eg structures. c) Images over periodic boundaries show how the -eg structures represent a poly-crystal.*

System	ρ(g/cm³)	N	ϕ(%)	n	l_B(Å)	α_L^{DM}(×10⁻⁶ K⁻¹)	α_L^{S}(×10⁻⁶ K⁻¹)	Θ_D(K)	B(GPa)	γ^{DM}	γ^{S}	B'
Nb-bcc	8.5	2	0.0	8.0±0.0	2.87±0.00	5.75	8.67	274.9	170.3	1.36	2.03	3.73
Nb-gb8.2	8.2	128	0.0	6.4±1.5	2.85±0.13	6.09	9.09	275.8	160.9	1.41	2.08	3.82
Nb-gb6.3	6.3	128	34.4	6.5±1.6	2.83±0.14	6.27	9.44	261.8	115.9	1.36	2.03	3.73
Nb-gb5.0	5.0	128	55.8	6.5±1.7	2.82±0.15	6.61	9.94	245.9	88.6	1.38	2.04	3.75
Nb-gb4.1	4.1	128	68.6	6.4±1.6	2.82±0.15	6.78	10.15	233.8	72.0	1.40	2.07	3.80
Nb-gb3.5	3.5	128	74.9	6.5±1.6	2.81±0.15	6.80	10.22	224.0	60.8	1.38	2.04	3.76
Nb+O-gb4.6	4.6	128	58.6	6.5±1.8	2.77±0.23	6.85	10.16	267.2	88.0	1.44	2.11	3.89
Cu-fcc	8.8	4	0.0	12.0±0.0	2.57±0.00	14.56	19.94	367.8	137.3	1.99	2.66	4.99
Cu-gb8.5	8.5	108	0.0	10.2±1.0	2.56±0.10	14.88	20.50	316.5	128.7	1.93	2.60	4.86
Cu-gb5.5	5.5	108	44.7	9.3±1.6	2.54±0.10	17.15	23.54	311.2	75.6	1.98	2.65	4.96
Nb-eg9	6.9	83	17.6	6.0±1.6	2.81±0.14	5.77	8.94	251.2	127.1	1.25	1.92	3.50
Nb-eg10	6.9	172	19.7	6.0±1.4	2.80±0.12	6.30	9.48	261.2	127.8	1.37	2.04	3.74
Nb-eg17	6.6	324	24.9	6.8±1.3	2.82±0.09	6.70	9.87	243.3	125.2	1.47	2.14	3.94

Table 4.2: *An overview of all systems investigated by DFT. The columns display the density, ρ, the number of atoms, N, the porosity, ϕ, the average coordination number, n, the average nearest neighbour bond length, l_B, the linear thermal expansion coefficient from Dugdale-MacDonald's approximation, α_L^{DM}, and from Slater's approximation, α_L^{S}, the Debye temperature, Θ_D, the bulk modulus, B, the Grüneisen parameter from Dugdale-MacDonald's approximation, γ^{DM}, and from Slater's approximation, γ^{S}, and the pressure derivative of the bulk modulus, B'.*

be explained by the inwards contraction of atoms at free pore surfaces. To insure that this pore formation is not only an artefact of missing neighbouring grains, we modelled under-dense, disordered GBs with the vapour-quench method in LAMMPS in between crystals of same ((100)) and different ((100),(110)) orientations, as well as in a solid foam-like structure, in which the GB component is fully surrounded by the crystalline component. Similar quantities of pores were observed for all these systems (depicted in Appendix section A.2). To assess the effect of experimentally found O incorporation, which might be preferably situated at the GBs (discussed in Section 4.3), one system (Nb+O-gb4.6) was constructed with 6.25% O impurities. α_L was calculated both from Dugdale-MacDonald's (DM) and Slater's (S) approximation for γ over a temperature range from 1 to 1300 K for Nb and to 700 K for Cu. A discussion on approximations for γ can be found in Appendix section A.1.

The change of α_L (DM-S average) with ρ for the bcc/fcc and -gb structures is illustrated in Figure 4.5 a). The single-crystalline systems exhibit the highest densities. Values for α_L of Nb reported in literature range from 6.8 to 8.5 [48, 64, 65] and α_L of Cu lies around 16.5 [63]. Comparing those to the calculated values in this study (cf. Table 4.2) shows that the experimental values are close to the average of DM and S approximations for Nb (α_L^{DM}=5.75, α_L^S=8.67) and
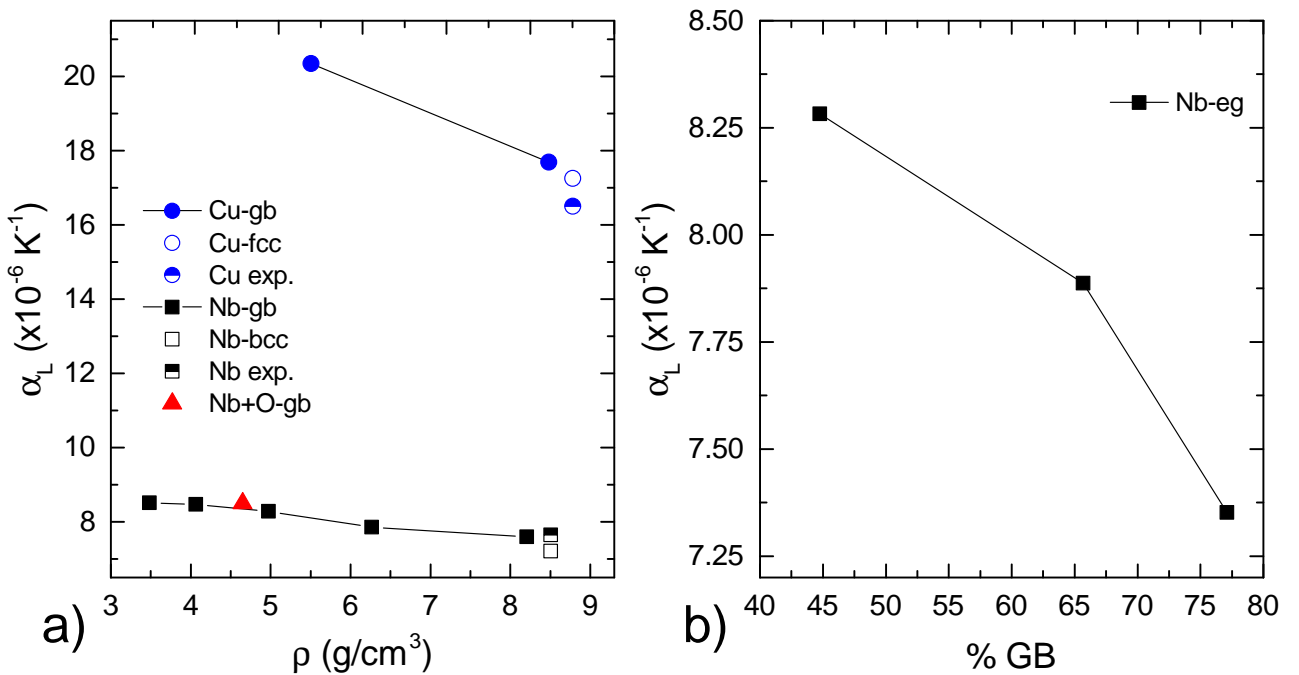

Figure 4.5: *a) DM-S averaged α_L vs. ρ for the -gb and bcc/fcc systems and experimental values [48, 63–65] and b) DM-S averaged α_L vs. %GB for the -eg systems.*

Cu (α_L^{DM}=14.56, α_L^{S}=19.94) and it can be concluded that the model performs well for the elemental crystals. Both approximations yield roughly the same trend, which is an increase in α_L with decreasing ρ. One observes an 18.0% increase in α_L for Nb from 7.21 to 8.51 at 8.5 to 3.5 g/cm^3 and an 17.9% increase for Cu from 17.25 to 20.34 at 8.8 to 5.5 g/cm^3, using the average of DM and S approximations. It can also be seen in Figure 4.5 a) that the system with O impurities exhibits a slightly higher ($\approx$0.2) expansion than pure Nb with comparable density. With an exemplarily rule-of-mixture calculation, mixing a -gb (Nb-gb4.1) system and crystalline bcc Nb (26% lower density, 50% GB), one obtains an increase in α_L of 8.7%, compared to single-crystalline Nb. Linearly fitting the α_L vs. ρ data, the effective α_L^{eff} can be expressed as a function of %GB, ρ_{GB} of the GB component, and the single-crystal α_L^{sc} as: $\alpha_L^{eff} =$ %GB/100($a\rho_{GB} + b$) + (1$-$%GB/100)α_L^{sc}, with a=-2.4x10^{-7}, b=9.4x10^{-6} for Nb and a=-7.8x10^{-7}, b=2.1x10^{-5} for Cu. Of course, such calculations do not really capture the character of GBs as interfaces between adjacent grains. The increase in α_L among the -gb systems is due to a decrease in Debye temperature, Θ_D, resulting from a decrease in bulk modulus, B, with increasing ϕ (cf. Table 4.2). Conceptually, one can picture that a lower Θ_D results in all phonon modes being energetically accessible at lower T, hence, enhancing thermal expansion. While the trend agrees with observations made by other authors (cf. Table 2.1), the magnitude is comparably low, as already found in the MD studies.

The -eg structures of Nb (see Figure 4.4 b) and c)) were chosen to have approximately one lattice parameter of GB between the grain and the cell boundary. The grains exhibit a Wulff-shape [66], whereat only (110) and (100) surfaces are considered due to the very small grain size. Since all grains, over periodic boundaries, have the same orientation, the GBs crystallized during relaxations at 0 K if they were too dense. As a consequence, we had to further decrease their density, which again resulted in pore formation. Furthermore, the smaller grains would lose their crystallinity during relaxation, which is why their relative positions had to be fixed. This gave rise to a slight compression of the intra-grain bonds at equilibrium V, while the bonds of the GB component were elongated so that the overall l_B stayed similar to the -gb systems (cf. Table 4.2).

The change of α_L with %GB for the -eg structures is shown in Figure 4.5 b). One can observe

a 11.2% decrease in α_L of Nb from 8.28 to 7.35 (DM-S average) with an increase in %GB from 44.6 to 77.1%. As already observed in the classical MD part of this work, the trend is the opposite of that reported in most previous studies reviewed in Section 2.1. In contrast to the -gb systems, Θ_D or B vary only insignificantly and non-monotonically among the -eg systems. With decreasing %GB, the increase in α_L results from a monotonic increase in γ, which itself originates from an increase in $B' = (\partial B/\partial P)_{P=0}$. This means that with a rise in pressure, P, the resistance against further compression becomes larger for systems with smaller %GB. One might wonder if this is an unphysical effect of the afore mentioned small compression of the intra-grain bonds that is more prominent the larger %GB is; but an already compressed bond would rather put up even more resistance against further compression, so this does not seem to play a role here. An explanation can be proposed based on the under-coordination of atoms in the porous GB. This under-dense part of the system can be expected to have a lower increase in B with advancing compression than the dense, full-coordinated crystalline grain. Accordingly, B' should decrease with increasing %GB. However, with the scarceness of reports describing an anti-proportional behaviour of α_L and %GB, some scepticism is appropriate. There are many approximations involved, not only for γ. The whole quasi-harmonic approach is based on Debye theory (discussed in brief in Appendix section A.1, see also [67]), which itself approximates the whole phonon dispersion as a linear extrapolation of small wave vector phonons' dispersion. Additionally, it is derived from crystal lattices. At large phonon wavelengths both crystalline and non-crystalline materials can be considered as elastic continua, but for wavelengths approaching interatomic distances, the concept of phonons is not thoroughly defined any more for non-crystalline solids and the dispersion would be smeared out with respect to a crystal. Also phonon scattering, e.g. at GBs is not considered in this model. Even without considering these approximation, the limited feasible number of atoms in DFT calculations makes it challenging to create representative systems.

In brief, we found the often reported (see Section 2.1) proportional relationship between the GB fraction and α_L for Nb and Cu. If a rule-of-mixture approach is applied, α_L increases up to 18%, depending on GB density, GB fraction, and chemical element, which can be attributed to a reduction of Debye temperature with decreasing density. For the -eg systems, similar to

the classical MD simulations of Nb, an anti-proportional relationship between %GB and α_L was predicted. Both MD simulations and the DFT Debye-Grüneisen approach for Nb possess some methodological limitations, such as inaccurate potentials, approximations and model systems, which challenge the counterintuitive results; therefore, experimental validation or refutation are essential.

4.3 Chemical and structural properties of Nb thin films

In order to study the chemical composition and the microstructural features of Nb thin films produced under varying deposition conditions, as described in Section 3.2, EDX and XRD measurements were carried out. Table 4.3 summarises the obtained results for the chemical composition and the peak evaluation based on Scherrer (Equation 2.4). The chemical composition of the different samples was found to be uniform, consisting of around 95-96 at% Nb, with a standard deviation below 0.5 at% (see Table 4.3). The samples contain around 5 at% of oxygen that may have been induced partially during deposition and, ex-situ, subsequently to the deposition process.

Figure 4.6 shows an exert of the diffraction peak pattern, focusing on the peaks hkl=110 a) and hkl=220 b), as no other peaks were obtained by XRD. Apparently, the samples consist of phase-pure bcc Nb. Furthermore, they exhibit a preferred (110) orientation. A shift of the peak position to lower angles upt to 0.34 ° is observed as the bias voltage increases. This can be explained by macro-strain, resulting from a homogeneous expansion of the lattice parameter [38, 43]. The diffraction signal of the (220) peak is visibly weaker than the one for the (110) peak. The small intensity leads to a hindered distinction of the actual peak from the background and makes the

Bias (-V)	Nb (at%)	O (at%)	(110) Peak			(220) Peak		
			2θ (°)	b (°)	D (nm)	2θ (°)	b (°)	D (nm)
10	95.2	4.8	38.57	0.20	43.13	82.64	0.36	29.20
50	94.7	5.4	38.56	0.21	40.05	82.62	0.39	27.49
100	95.8	4.3	38.52	0.22	37.85	82.53	0.43	24.67
150	96.0	4.0	38.48	0.26	32.94	82.43	0.55	19.22
200	95.6	4.4	38.42	0.32	25.99	82.30	0.77	13.68

Table 4.3: *Chemical composition, diffraction peak position, 2θ, width, b, and estimated grain size, D, of Nb thin films obtained under varying coating conditions.*
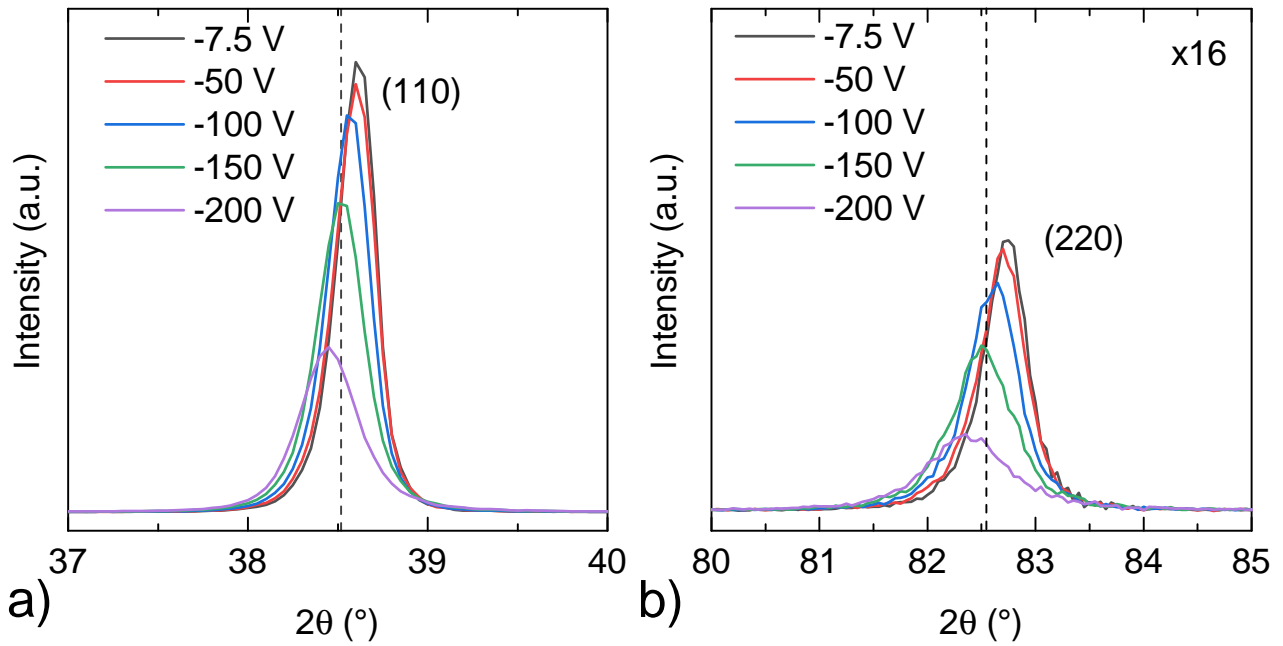
Figure 4.6: *Diffraction peaks of Nb thin film samples with changing bias voltage around the positions of the a) (110) peak and b) (220) peak (intensity multiplied by 16).*

signal sensible to instrumental broadening (cf. Section 2.3). Hence, the resulting grain sizes are significantly smaller (see Figure 4.7 a)).

The calculation results for the mean grain size obtained with the Scherrer equation for hkl=110 and hkl=220 are resumed in Table 4.3. A decrease in the average grain size from 43.13 nm to 25.99 nm with an increase of the negative bias voltage from 10 V to 200 V is observed (see Figure 4.7 a)). Supposedly, the high acceleration speed of ionised incident particles, achieved by an increasing bias voltage, leads to a magnified ion bombardment, which causes a higher defect concentration. In consequence, renucleation of grains is favoured and the grain size decreases [40, 68].

Since in the Scherrer approach, all peak broadening is ascribed to grain size effects and micro-strains are neglected (cf. Section 2.3), further analyses by means of the Williamson and Hall method were carried out to estimate the broadening portion due to micro-strain. Table 4.4 shows the resulting mean grain sizes obtained by the Williamson and Hall plot. Additionally, micro-strain and residual stress (calculated with E and ν from ab initio calculations) are resumed. The final grain size in all the samples are up to 50% smaller than the first estimation by the Scherrer equation. The amount of negative residual micro-stress increases from 0.036 MPa to 0.047 MPa, as the negative bias voltage increases from 10 V to 200 V (see Figure 4.7 b)). The effect might be caused by higher
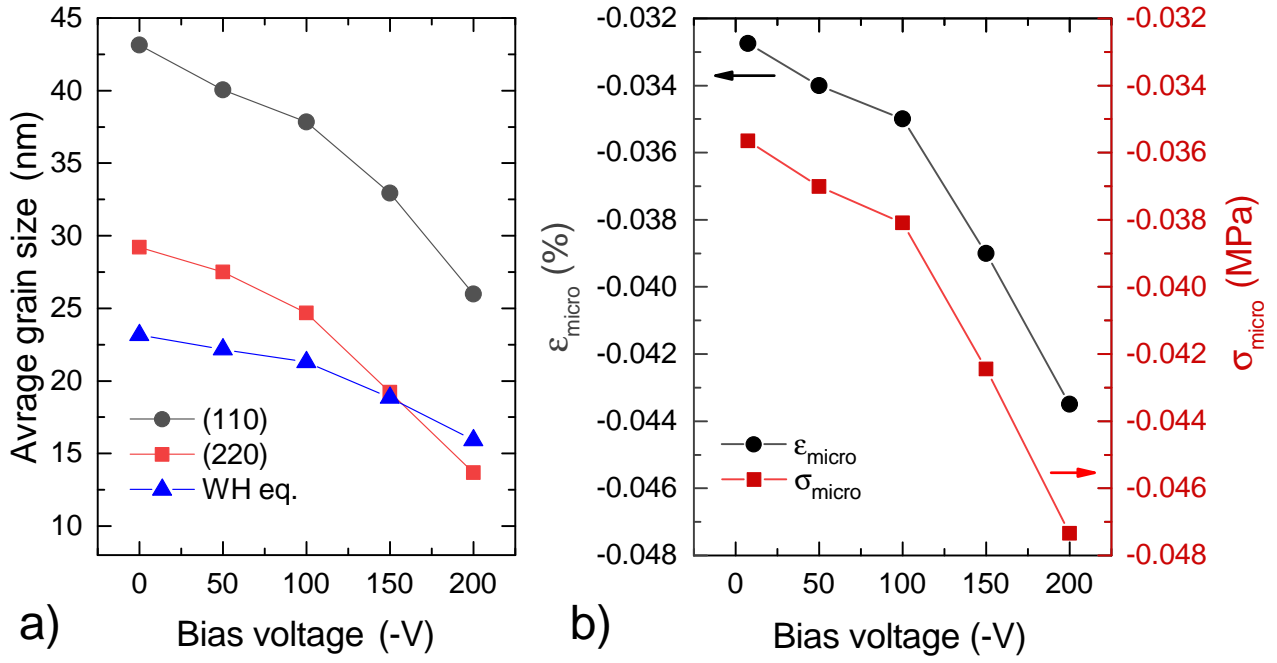
Figure 4.7: *a) Average grain size according to Scherrer ((110),(220)) and Williamson-Hall equations and b) micro-strain and micro-stress calculated from Williamson-Hall equation.*

acceleration speeds and impact pressures of incident particles during deposition. The observed trend is augmented for negative bias voltages larger than 100 V (see Figure 4.7 b)). This leads to a change in the grain size trend for high bias voltages. The grain size decrease declines between -100 V and -200 V from -0.1186 nm/V to -0.0538 nm/V, after applying the Williamson and Hall approach (see Figure 4.7 b)). Regarding the basic assumptions of the Williams and Hall method as they were discussed in Section 2.3, the obtained grain sizes and the micro-strains have to be regarded critically, since the given samples show a sharp texture and most likely exhibit anisotropic strain. Furthermore, the Williamson and Hall plot was based on no more than two peaks of which the (220) peak had a comparably weak intensity.

Bias (-V)	D_{WH}	D_{Sch}	ϵ (%)	σ (MPa)
10	23.15	43.13	-0.033	-0.036
50	22.18	40.05	-0.034	-0.037
100	21.30	37.84	-0.035	-0.038
150	18.84	32.94	-0.039	-0.042
200	15.92	25.99	-0.044	-0.047

Table 4.4: *For samples with varying bias: Slope and Y-axis intercept of Williamson-Hall plot, average grain size obtained with Williamson-Hall, D_{WH}, and Scherrer equation, D_{Sch}, micro-strain, ϵ, and residual stress, σ, after Williamson and Hall.*

Concluding, we found the chemical composition of the Nb thin films to be nearly uniform among all samples, with O impurities of around 5 at% and a deviation of less than 0.5 at%. The analysed XRD peak patterns showed a pure Nb bcc structure with a (110) texture. Furthermore, the intrinsic stress was estimated and lead to a correction of the grain size trend. The residual micro-stress, obtained by means of the W-H equation (Equation 2.6), increased by 23.4% and the grain size based on Scherrer and Williamson and Hall decreases by 40 to 32%, respectively, when the bias voltage increases from floating (-10) to -200 V.

5. Conclusion

The goal of this work was to study grain size-dependent thermal expansion at the examples of Nb and Cu with different computational approaches, as well as to create a basis for an experimental investigation of this effect in Nb thin films. Therefore, we have reviewed previous studies on grain size dependency of the thermal expansion and found that the reported differences range from almost zero [11] to more than hundred [14] percent and that thermal expansion is also influenced by sample-specific factors such as residual stresses, porosity, microstructural and phase changes, or chemical composition.

The grain size dependency of the thermal expansion coefficient of Nb and Cu were investigated computationally via molecular dynamics and ab initio electronic structure calculations within the framework of the quasi-harmonic Debye-Grünseisen model. MD simulations of single-crystalline Cu yield $\alpha_L^{corr} \approx 16.5 \times 10^{-6}$ K^{-1} in agreement with experiment [63]. Cu systems with grain boundary fractions increasing from 0 to 58.2% show an increase in α_L^{corr} of 8.7%. This trend coincides with experimental results from other studies on Cu, even though its magnitudes is small compared to a 20 to 100% increase reported in literature [5, 12]. The high values in these studies, as reviewed in Section 2.1, might partly be correlated to synthesis-specific sample properties, such as porosity or residual stresses. MD simulations of single crystalline Nb output $\alpha_L^{corr} \approx 9.1 \times 10^{-6}$ K^{-1}, which is higher than experimental $\alpha_L \approx 8.5 \times 10^{-6}$ K^{-1} [48]. In contrast to Cu, Nb systems with grain boundary fractions increasing from 0 to 67.5% result in an overall temperature-averaged decrease in α_L^{corr} of 3.7%, while over a temperature range from 100 to 300 K, an increase in α_L^{corr} of about 5% can still

be observed. The reversal of the trend at higher temperatures might be an artefact of the employed Nb potential, which does not reproduce the high-energy phonon dispersion correctly [48].

The Debye-Grüneisen approach with Slater's and Dugdale-MacDonald's approximations for the Grüneisen parameter yields averaged values for α_L that lie closely around reported experimental data [48, 63–65]. Disordered, under-coordinated and under-dense systems of Nb and Cu were created to resemble GBs in ab initio simulations. With decreasing density, α_L increased in these systems, which can be attributed to a decreasing Debye temperature. An exemplarily rule-of-mixture calculation with such a system and crystalline bcc Nb (26% lower density, 50% GB) yields an increase in α_L of 8.7%, which is similar in magnitude to results from MD simulations of Nb at low temperatures and Cu. Embedded grain systems in ab initio simulations reveal a decrease in α_L with increasing grain boundary fraction that emerges from larger Grüneisen parameters. Though, this can be reasoned with the higher compressibility of the GB component within the model, the counterintuitive trend might be a consequence of approximations made and potentially unrepresentative model systems.

Nb thin films of about 1 μm thickness were deposited on Si substrates via DC magnetron sputtering with substrate bias varying from floating (-10 V) to -200 V. All samples consist of pure bcc Nb with an oxygen concentration of around 5 at% exhibiting a preferred (110) orientation. A decrease in average grain size, based on Scherrer and Williamson and Hall, of approximately 40 to 32%, respectively, with increasing negative bias from floating (-10 V) to -200 V is observed, and the residual micro-stresses obtained by the Williamson-Hall equation are small, (on average 0.037 MPa) relative to the materials yield stress. Accordingly, the Nb thin film samples are well suited for upcoming thermal expansion studies by wafer curvature method.

6. Outlook

The next step in the experimental procedure would be to determine the elastic modulus of the deposited thin films by nano-indentation and continue with the wafer curvature measurements. The experiments could then be repeated for Cu and, as Nb seems to behave special in the simulations, it would be interesting to further investigate other material systems experimentally. Also, with the obtained experimental data for α_L, the computational results can be revised concerning the validity

of the used model and the assumptions made.

Moreover, scanning transmission electron microscopy (STEM) or TEM measurements could be carried out with the produced samples to verify the results of the grain size approximation by the Scherrer and Williamson-Hall equations. This would also allow for the consideration of the type of microstructure, i.e. columnar or equiaxed grains, and its influence on α_L.

The MD simulations in this work have shown that it is feasible to study D-dependent thermal expansion computationally. To investigate if the results for Nb are biased by an inaccurate potential or if they really are physical, it would be intriguing to see if other elemental poly-crystals exhibit a similar behaviour. Therefore, a large-scale systematic study of this kind, throughout the periodic table, is desirable, also to uncover potential dependencies on crystal structure, atomic weight, grain boundary density, etc. A limiting factor is, of course, the availability and accuracy of interatomic potentials.

Ab initio simulations in this work support the frequently spearheaded argument that lower density and atomic coordination come along with higher thermal expansion; however, limited amounts of atoms in these simulations prohibit the generation of actual poly-crystalline structures. There exist some modern linear-scaling DFT codes [69, 70] that allow for some tens of thousands of atoms (which would still not be quite enough), but at the price of lower accuracy and enormous computational and time costs. While the Debye-Grünseisen approach in conjunction with ab initio simulations has proven to work well for elemental [17, 71–73] and compound [74] single-crystals, its usefulness has yet to be assessed experimentally for our purpose.

7. Acknowledgements

8. Declaration of originality

We, Pascal Bliem (sections Abstract, 1.0, 2.1, 3.1, 4.1, 4.2, 5.0, 6.0, A1, A2, and A3), Oliver Beyß (sections 2.2, 3.2, 4.3, 5.0 and 6.0), and Fatim-Zahra Mouhib (sections 2.3, 3.2, 4.3, and 5.0), confirm that, unless stated otherwise, this work is the result of our own efforts. These efforts include the originality of written works as well as diagrams or similar pictorial material and results. Where material is drawn from elsewhere, references are included.

(Pascal Bliem)   (Oliver Beyß)   (Fatim-Zahra Mouhib)

9. References

[1] Nix, W. D. *Metallurgical Transactions A* **20**(11), 2217 (1989).

[2] Fitzsimmons, M. R., Burkel, E., and Sass, S. L. *Physical Review Letters* **61**, 2237–2240 (1988).

[3] Wagner, M. *Physical Review B* **45**, 635–639 (1992).

[4] Zhu, Y. F., Lian, J. S., and Jiang, Q. *The Journal of Physical Chemistry C* **113**(39), 16896–16900 (2009).

[5] Klam, H., Hahn, H., and Gleiter, H. *Acta Metallurgica* **35**(8), 2101 – 2104 (1987).

[6] Rupp, J. and Birringer, R. *Physical Review B* **36**, 7888–7890 (1987).

[7] Eastman, J. A., Fitzsimmons, M. R., and Thompson, L. J. *Philosophical Magazine Part B* **66**(5), 667–696 (1992).

[8] Sui, M. and Lu, K. *Nanostructured Materials* **6**(5), 651 – 654 (1995). Proceedings of the Second International Conference on Nanostructured Materials.

[9] Lu, K. and Sui, M. *Acta Metallurgica et Materialia* **43**(9), 3325 – 3332 (1995).

[10] Zhao, Y. H. and Lu, K. *Physical Review B* **56**, 14330–14337 (1997).

[11] Turi, T. and Erb, U. *Materials Science and Engineering: A* **204**(1), 34 – 38 (1995). Proceedings of the Symposium on Engineering of Nanostructured Materials.

[12] Kuru, Y., Wohlschlögel, M., Welzel, U., and Mittemeijer, E. J. *Applied Physics Letters* **90**(24), 243113 (2007).

[13] Daniel, R., Holec, D., Bartosik, M., Keckes, J., and Mitterer, C. *Acta Materialia* **59**(17), 6631 – 6645 (2011).

[14] Fang, W. and Lo, C.-Y. *Sensors and Actuators A: Physical* **84**(3), 310 – 314 (2000).

[15] Rapaport, D. C., Blumberg, R. L., McKay, S. R., Christian, W., et al. *Computers in Physics* **10**(5), 456–456 (1996).

[16] Martin, R. M. *Electronic structure: basic theory and practical methods*. Cambridge university press, (2004).

[17] Moruzzi, V. L., Janak, J. F., and Schwarz, K. *Physical Review B* **37**, 790–799 (1988).

[18] Gottstein, G. *Materialwissenschaft und Werkstofftechnik: Physikalische Grundlagen*. Springer-Verlag, (2013).

[19] Wolf, D., Yamakov, V., Phillpot, S., Mukherjee, A., and Gleiter, H. *Acta Materialia* **53**(1), 1 – 40 (2005).

[20] Meyers, M., Mishra, A., and Benson, D. *Progress in Materials Science* **51**(4), 427 – 556 (2006).

[21] Ohring, M. *Materials science of thin films*. Academic press, (2001).

[22] Gleiter, H. *Acta Materialia* **48**(1), 1 – 29 (2000).

[23] Ganapathi, S. and Rigney, D. *Scripta Metallurgica et Materialia* **24**(9), 1675 – 1678 (1990).

[24] Thomas, G., Siegel, R., and Eastman, J. *Scripta Metallurgica et Materialia* **24**(1), 201 – 206 (1990).

[25] Holzapfel, D. M. Master's thesis, RWTH Aachen University, (2016).

[26] Saringer, C., Tkadletz, M., and Mitterer, C. *Surface and Coatings Technology* **274**, 68 – 75 (2015).

[27] Zhao, Z., Hershberger, J., Yalisove, S., and Bilello, J. *Thin Solid Films* **415**(1), 21 – 31 (2002).

[28] Mézin, A. and Hemel, A. *Surface and Coatings Technology* **258**, 1128 – 1136 (2014).

[29] Hsieh, C., Chen, C., Chen, C., and Liao, M. *Procedia Engineering* **79**, 323 – 327 (2014). 37th National Conference on Theoretical and Applied Mechanics (37th NCTAM 2013) & The 1st International Conference on Mechanics (1st ICM).

[30] Ouled-Khachroum, T., Richard, M.-I., Noé, P., Guichet, C., Mocuta, C., Sabbione, C., Hippert, F., and Thomas, O. *Thin Solid Films* **617**, 44 – 47 (2016). European Materials Research Society Spring Meeting 2015.

[31] Lei, S., Huang, J.-H., and Chen, H. *Materials Chemistry and Physics* **199**, 185 – 192 (2017).

[32] Scherrer, P. *Nachrichten von der Gesellschaft der Wissenschaften zu Göttingen, Mathematisch-Physikalische Klasse* **1918**, 98–100 (1918).

[33] Birkholz, M. *Thin film analysis by X-ray scattering*. John Wiley & Sons, (2006).

[34] Langford, J. I. and Wilson, A. J. C. *Journal of Applied Crystallography* **11**(2), 102–113 (1978).

[35] Daniel, R., Zeilinger, A., Schöberl, T., Sartory, B., Mitterer, C., and Keckes, J. *Journal of Applied Physics* **117**(23), 235301 (2015).

[36] v. Laue, M. *Annalen der Physik* **417**(6), 569–576 (1936).

[37] Patterson, A. L. *Physical Review* **56** (1939).

[38] Weibel, A., Bouchet, R., Boulc', F., and Knauth, P. *Chemistry of materials* **17**(9), 2378–2385 (2005).

[39] Mittemeijer, E. J. and Welzel, U. *Zeitschrift für Kristallographie International journal for structural, physical, and chemical aspects of crystalline materials* **223**(9), 552–560 (2008).

[40] Kumar, M. and Mitra, R. *Surface and Coatings Technology* **251**, 239 – 246 (2014).

[41] Wang, A.-N., Huang, J.-H., Hsiao, H.-W., Yu, G.-P., and Chen, H. *Surface and Coatings Technology* **280** (2015).

[42] Wang, A.-N., Chuang, C.-P., Yu, G.-P., and Huang, J.-H. *Surface and Coatings Technology* **262** (2015).

[43] Cullity, B. D. and Weymouth, J. W. *American Journal of Physics* **25**(6), 394–395 (1957).

[44] Williamson, G. and Hall, W. *Acta Matellurgica* **1**, 21–31 (1953).

[45] Prabhu, Y. and Rao, K. *World Journal of Nano Science and Engineering* **4**, 21–28 (2014).

[46] Borchert, H., Shevchenko, E. V., Robert, A., Mekis, I., Kornowski, A., Grübel, G., and Weller, H. *Langmuir* **21**(5), 1931–1936 (2005).

[47] Plimpton, S. *Journal of Computational Physics* **117**(1), 1 – 19 (1995).

[48] Fellinger, M. R., Park, H., and Wilkins, J. W. *Physical Review B* **81**, 144119 (2010).

[49] Mishin, Y., Mehl, M. J., Papaconstantopoulos, D. A., Voter, A. F., and Kress, J. D. *Physical Review B* **63**, 224106 (2001).

[50] Hirel, P. *Computer Physics Communications* **197**, 212 – 219 (2015).

[51] Stukowski, A. *Modelling and Simulation in Materials Science and Engineering* **18**(1), 015012 (2010).

[52] Stukowski, A. *Modelling and Simulation in Materials Science and Engineering* **20**(4), 045021 (2012).

[53] Ozaki, T. *Physical Review B* **67**, 155108 (2003).

[54] Perdew, J. P., Burke, K., and Ernzerhof, M. *Physical Review Letters* **77**, 3865–3868 (1996).

[55] Kresse, G. and Furthmüller, J. *Physical Review B* **54**, 11169–11186 (1996).

[56] Methfessel, M. and Paxton, A. T. *Physical Review B* **40**, 3616–3621 (1989).

[57] Murnaghan, F. *Proceedings of the National Academy of Sciences* **30**(9), 244–247 (1944).

[58] Birch, F. *Physical Review* **71**, 809–824 (1947).

[59] Monkhorst, H. J. and Pack, J. D. *Physical Review B* **13**, 5188–5192 (1976).

[60] Slater, J. C. *Introduction to chemical physics*. McGraw Hill New York, (1939).

[61] Dugdale, J. S. and MacDonald, D. K. C. *Physical Review* **89**, 832–834 (1953).

[62] Jones, E., Oliphant, T., Peterson, P., et al. (2001). SciPy: Open source scientific tools for Python (http://www.scipy.org/).

[63] Nix, F. C. and MacNair, D. *Physical Review* **60**, 597–605 (1941).

[64] Roberge, R. *Journal of the Less Common Metals* **40**(1), 161 – 164 (1975).

[65] Edwards, J. W., Speiser, R., and Johnston, H. L. *Journal of Applied Physics* **22**(4), 424–428 (1951).

[66] Wulff, G. *Zeitschrift für Kristallographie* **34**, 449–530 (1901).

[67] Kittel, C. *Introduction to solid state physics*. Wiley, (2005).

[68] Park, J.-K., Lee, W.-S., and Baik, Y.-J. *Surface and Coatings Technology* **171**(1), 1 – 5 (2003). Proceedings from the Joint International Symposia of the 6th APCPST, 15th SPSM, 4th International Conference on Open Magnetic Sytems for Plasma Confinement and 11th KAPRA.

[69] Hine, N., Haynes, P., Mostofi, A., Skylaris, C.-K., and Payne, M. *Computer Physics Communications* **180**(7), 1041 – 1053 (2009).

[70] Ozaki, T. *Physical Review B* **74**, 245101 (2006).

[71] Lu, X.-G., Selleby, M., and Sundman, B. *Acta Materialia* **53**(8), 2259 – 2272 (2005).

[72] Söderlind, P., Nordström, L., Yongming, L., and Johansson, B. *Physical Review B* **42**, 4544–4552 (1990).

[73] Söderlind, P. and Johansson, B. *Thermochimica Acta* **218**, 145 – 153 (1993).

[74] Music, D., Geyer, R. W., and Keuter, P. *Applied Physics Letters* **109**(22), 223903 (2016).

[75] Grüneisen, E. *Annalen der Physik* **344**(12), 257–306 (1912).

[76] Vočadlo, N. and Price, G. D. *Physics of the Earth and Planetary Interiors* **82**(3), 261 – 270 (1994).

[77] Hill, R. *Journal of the Mechanics and Physics of Solids* **11**(5), 357 – 372 (1963).

[78] Music, D., Takahashi, T., Vitos, L., Asker, C., Abrikosov, I. A., and Schneider, J. M. *Applied Physics Letters* **91**(19), 191904 (2007).

[79] Cottenier, S. (2016). Computational Materials Physics: a hands-on guide to meaningful quantum simulations for materials (http://www.compmatphys.org/).

[80] Hohenberg, P. and Kohn, W. *Physical Review* **136**, B864–B871 (1964).

[81] Kohn, W. and Sham, L. J. *Physical Review* **140**, A1133–A1138 (1965).

[82] Perdew, J. P., Chevary, J. A., Vosko, S. H., Jackson, K. A., Pederson, M. R., Singh, D. J., and Fiolhais, C. *Physical Review B* **46**, 6671–6687 (1992).

[83] Becke, A. D. *Physical Review A* **38**, 3098–3100 (1988).

[84] Lee, C., Yang, W., and Parr, R. G. *Physical Review B* **37**, 785–789 (1988).

[85] Ibach, H. and Lüth, H. *Festkörperphysik: Einführung in die Grundlagen*. Springer-Verlag, (2009).

[86] Ashcroft, N. W., Mermin, N. D., and Gress, J. *Festkörperphysik*, volume 3. Oldenbourg, (2013).

[87] Giannozzi, P., Baroni, S., Bonini, N., Calandra, M., Car, R., Cavazzoni, C., Ceresoli, D., Chiarotti, G. L., Cococcioni, M., Dabo, I., Corso, A. D., de Gironcoli, S., Fabris, S., Fratesi, G., Gebauer, R., Gerstmann, U., Gougoussis, C., Kokalj, A., Lazzeri, M., Martin-Samos, L., Marzari, N., Mauri, F., Mazzarello, R., Paolini, S., Pasquarello, A., Paulatto, L., Sbraccia, C., Scandolo, S., Sclauzero, G., Seitsonen, A. P., Smogunov, A., Umari, P., and Wentzcovitch, R. M. *Journal of Physics: Condensed Matter* **21**(39), 395502 (2009).

[88] Slater, J. C. *Physical Review* **51**, 846–851 (1937).

[89] Andersen, O. K. *Physical Review B* **12**, 3060–3083 (1975).

[90] Blaha, P., Schwarz, K., Madsen, G., Kvasnicka, D., and Luitz, J. *WIEN2k: An augmented plane wave+ local orbitals program for calculating crystal properties*. Karlheinz Schwarz, Technische. Universitat Wien Wien, Austria, (2001).

[91] Blöchl, P. E. *Physical Review B* **50**, 17953–17979 (1994).

[92] Singh, D. *Physical Review B* **43**, 6388–6392 (1991).

A. Appendix

A.1 Debye-Grüneisen model

With an expression for the free energy of a solid, F, as a function of temperature, T, and volume, V, one can determine the equilibrium V at different T, and hence, calculate thermal expansion. Combining Debye and Grüneisen theory yields a quasi-harmonic expression for F which, to the authors' knowledge, was first used by Moruzzi et al. [17]. Since then, the approach was successfully used for elemental crystals [17, 71–73] and crystalline compounds [74]. In this work, we mostly follow the scheme derived by Söderlind et al. [72]. Considering the total ground state energy, E_{tot}, and the energy, E_{ph}, and entropy, S_{ph}, contributions of phonons according to Debye theory, one obtains:

$$
\begin{aligned}
F(V,T) &= E_{tot}(V) + E_{ph}(V,T) - TS_{ph}(V,T) \\
&= E_{tot}(V) - k_B N T \left[3 \left(\frac{T}{\Theta_D} \right)^3 \int_0^{\Theta_D/T} \frac{x^3}{e^x - 1} dx - \ln(1 - e^{-\Theta_D/T}) - \frac{9\Theta_D}{8T} \right],
\end{aligned}
\tag{A.1}
$$

where k_B is the Boltzmann constant, N is the number of atoms, and Θ_D is the Debye temperature. This neglects electron-phonon coupling, electron entropy, as well as the change of electronic structure with temperature. Lu et al. [71] proposed additional expressions for electronic entropy and excitations. These corrections were shown to be relevant at high T but negligible at moderate T, which is why we do not consider them here. $\Theta_D = \hbar \omega_D / k_B$ depends on the highest phonon cutoff frequency $\omega_D = (6\pi^2 v_m^2/V)^{1/3}$, which depends on the mean velocity of sound v_m (here $\hbar$ is the reduced Planck constant and V is the Wigner-Seitz volume). Assuming an isotropic crystal, one can obtain the ground state Debye temperature by:

$$
\Theta_{D0} = \frac{h}{k_B} \left(\frac{4\pi}{3} \right)^{-1/6} \left[\frac{2}{3} \left(\frac{2}{1-2\nu} \right)^{3/2} + \frac{1}{3} \left(\frac{1}{1-\nu} \right)^{3/2} \right]^{-1/3} \left(\frac{3}{1+\nu} \right)^{1/2} \left(\frac{rB}{M} \right)^{1/2},
\tag{A.2}
$$

where ν is Poisson's ratio, r is the Wigner-Seitz radius, B is the bulk modulus, each calculated for the ground state, and M is the atomic mass. However, Debye theory only considers harmonic vibrations, which would not cause any expansion. An anharmonic volume dependence of Θ_D can be obtained as $\Theta_D(r, r_0) = \Theta_{D0}(r_0/r)^{3\gamma}$, by introducing the Grüneisen parameter, γ. In principle, there is an individual $\gamma_i(q) = -\partial \ln \omega(q)_i / \partial \ln V$ for every phonon mode with a wave vector, q, in

the first Brillouin zone [75]. To avoid a full phonon calculation, approximation formulas of the form $\gamma = aB' - b$ are often used, in which $B' = (\partial B/\partial P)_{P=0}$ is the first pressure derivative of the bulk modulus and a and b are constants. Two of these approximations derived from Debye theory, named after Slater (S) [60] (a=0.5, b=1/6) and Dugdale-MacDonald (DM) [61] (a=0.5, b=0.5), have shown to deliver results close to experiment [17, 71–74], and were critically reviewed by Vočadlo et al. [76]. Slater's relation is only valid if ν is independent of V (or P), which is fundamentally impossible for purely geometric reasons. The DM model considers a V-dependence of ν as $\partial \nu / \partial V = -1/3 V_0^{-1/3} V^{2/3}$, but assumes a one-dimensional lattice, and therefore, only longitudinal vibrational modes [76]. Vočadlo et al. compared these approximations to lattice dynamics calculations of different lattice types with varying interaction ranges and concluded that none of them performs universally well and that some approximations are more suitable for certain materials than others.

The input data for this model is obtained from ab initio electronic structure calculations. E vs. V data is fitted with a Birch-Murnaghan equation of state [57, 58], from which E_0, V_0, B_0, and B' can be obtained as fitted parameters. ν is calculated from elastic constants using the Hill (Reuss-Voigt average) method [77]. Cubic elastic constants were calculated, as proposed by Music et al. [78], by applying the volume-conserving distortions

$$D = \begin{pmatrix} 1+\delta & 0 & 0 \\ 0 & 1-\delta & 0 \\ 0 & 0 & (1-\delta^2)^{-1} \end{pmatrix}, \quad \text{and} \quad D_{44} = \begin{pmatrix} 1 & \delta_{44} & 0 \\ \delta_{44} & 1 & 0 \\ 0 & 0 & (1-\delta_{44}^2)^{-1} \end{pmatrix}, \quad \text{(A.3)}$$

with δ probed from -0.02 to 0.02 in 0.05 steps. With the relationship $B = 1/3(C_{11} + 2C_{12})$, the elastic constants can be obtained from quadratic fits of $\Delta E = V(C_{11} - C_{12})\delta^2 + O(\delta^4)$ vs. δ and $\Delta E_{44} = 2VC_{44}\delta_{44}^2 + O(\delta_{44}^4)$ vs. δ_{44} data. For non-crystalline simulation cells, the energy minimum did not always lie around δ, δ_{44}=0, depending on the direction of the distortions. The distortions were then applied along three symmetry-equivalent directions and the results were averaged. This cubic approach was also used for non-crystalline systems in cubic simulation cells to assess their degree of isotropy by the isotropy condition $C_{44} = (C_{11} - C_{12})/2$. For none of the non-crystalline system did $(C_{11} - C_{12})/2$ differ more than 7.5% from C_{44}, except one (23.8% for Cu-gb5.5).

A.2   Additional vapour-quenched GB structures

To insure that the pore formation in the -gb structures discussed in Section 4.2 is not only an artefact of missing neighbouring grains, we modelled under-dense, disordered Nb GBs with the vapour-quench method (described in Section 3.1) in LAMMPS. GBs (coloured in gold) in between grains (coloured in green) of same ((100)) orientations are shown in Figure A.1. GBs in between grains of different ((100) vs. (110)) orientations are shown in Figure A.2. A solid foam-like structure, in which the GB component is fully surrounded by the crystalline component, is shown in Figure A.2.
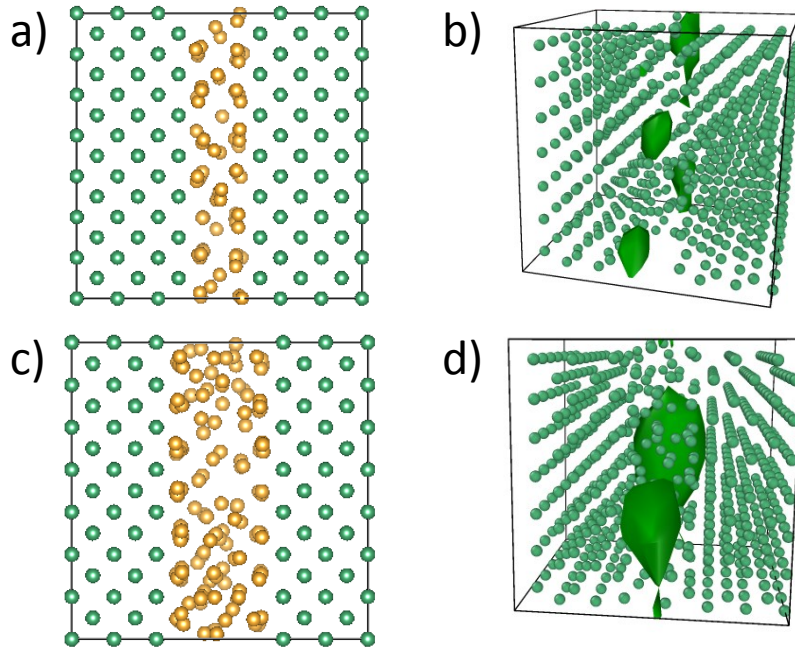

Figure A.1: *a) A Nb GB (one lattice parameter thickness, coloured in gold) in between (100) oriented grains (coloured in green). b) The surface mesh is used to indicate pores within the GB with one lattice parameter thickness. c) A Nb GB (two lattice parameter thickness, coloured in gold) in between (100) oriented grains (coloured in green). b) The surface mesh is used to indicate pores within the GB with two lattice parameter thickness.*
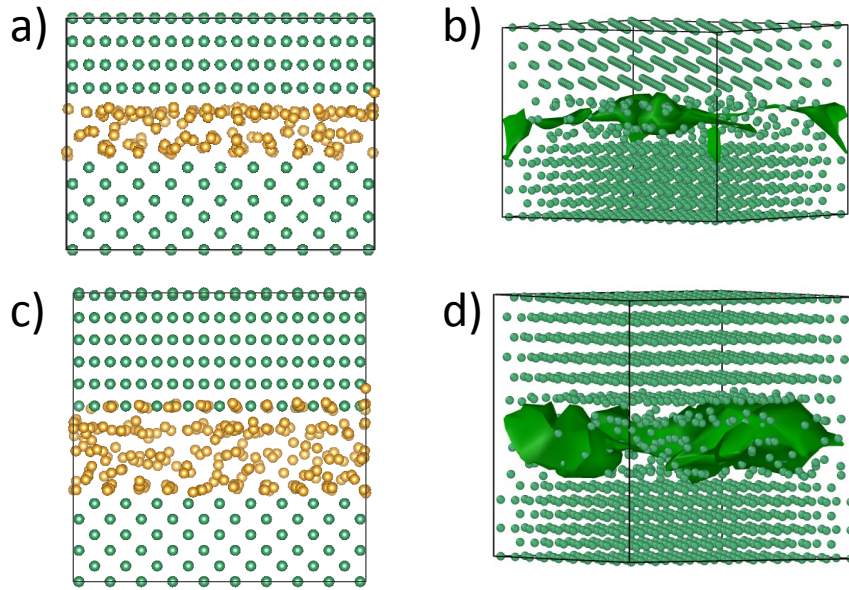
Figure A.2: *a) A Nb GB (one lattice parameter thickness, coloured in gold) in between (100) and (110) oriented grains (coloured in green). b) The surface mesh is used to indicate pores within the GB with one lattice parameter thickness. c) A Nb GB (two lattice parameter thickness, coloured in gold) in between (100) and (110) oriented grains (coloured in green). b) The surface mesh is used to indicate pores within the GB with two lattice parameter thickness.*
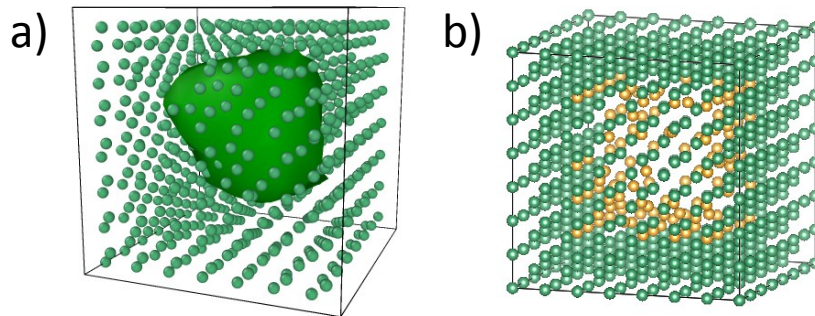

Figure A.3: *a) A solid foam-like structure, in which the GB component (coloured in gold) is fully surrounded by the crystalline component (coloured in green). b) The surface mesh is used to indicate a pore.*

A.3 Introduction to density functional theory

This appendix provides a short introduction to density functional theory (DFT), focusing more on the concepts involved in an actual DFT calculation than on the mathematics behind it; some mathematics will of course be needed. Regarding the story line, it follows, to a large extent, a course on computational materials physics [79] given by Stefaan Cottenier at the University of Gent in Belgium. Where a specific concept can be attributed to individual contributions, the respective

papers will be cited. A very comprehensive overview on the many different methods used in DFT framework can be found e.g. in R. M. Martin's book "Electronic structure: basic theory and practical methods" [16].

Density functional theory is nowadays the most popular way to perform electronic structure calculations. We will see that it states that a system's ground state is uniquely determined by the electron density and that this reduces a N-electron problem from 3N spatial degrees of freedom to only the 3 spatial degrees of freedom of the electron density (neglecting spin). Thereby, it provides a framework to efficiently calculate the electronic structure of materials from first principles or ab initio, which means without the input of empirical data.

Before we start with DFT we have to cover some basic quantum mechanics to provide a sound basis for further concepts. The first foundation is the Schrödinger equation:

$$H\Psi = E\Psi. \tag{A.4}$$

It is in general an eigenvalue equation and the starting point of any quantum mechanical description of a many-particle problem. It consists of three parts: the Hamiltonian, the wave function, and the energy eigenvalue. The Hamiltonian, H, is an operator which corresponds to the total energy of the system. Therefore, it has to describe all interactions in a system. If we consider a material consisting of atomic nuclei and electrons (neglecting strong and weak interactions in the nuclei, gravity, or interactions with the Higgs field) the Hamiltonian will look like:

$$\begin{aligned} H = & -\hbar^2 \sum_A \frac{\nabla_{\vec{R}_A}^2}{2M_A} - \hbar^2 \sum_i \frac{\nabla_{\vec{r}_i}^2}{2m_i} + \frac{1}{2}\frac{e^2}{4\pi\epsilon_0} \sum_{A\neq B} \frac{Z_A Z_B}{|\vec{R}_A - \vec{R}_B|} \\ & - \frac{1}{2}\frac{e^2}{4\pi\epsilon_0} \sum_{i\neq j} \frac{1}{|\vec{r}_i - \vec{r}_j|} - \frac{e^2}{4\pi\epsilon_0} \sum_{i,A} \frac{Z_A}{|\vec{r}_i - \vec{R}_A|}. \end{aligned} \tag{A.5}$$

Here, upper case letters are used for nuclei and lower case letters for electrons. The sums go over all nuclei and all N electrons. $\hbar$ is the reduced Plank constant, m and M are masses, $\vec{r}$ and $\vec{R}$ are position vectors, e is the unit charge, Z are nuclear charges, and ϵ_0 is the vacuum permittivity. The individual terms correspond to the kinetic energy of nuclei and electrons, and the electrostatic (Coulomb) interaction between nuclei and nuclei, electrons and electrons, and nuclei and electrons, respectively. The second part in Equation A.4 is the wave function, Ψ. It is not a physical observable and has many interpretations throughout quantum mechanics; however, it contains everything we

can know about the system, all states the system can be in. As a function, it maps a set of input values to a set of allowable (complex) output values so that each input has exactly one output. For N particles with 3 spatial degrees of freedom this means $\Psi : (\mathbb{R}^3)^N \to \mathbb{C}$ without spin or $\Psi : (\mathbb{R}^3)^N \otimes \mathbb{C}^{[(2s+1)\times 1]^N} \to \mathbb{C}$ with spin. An important axiom regarding the wave function is that it is antisymmetric for fermion exchange (electrons are fermions), which means that it has to change sign when the particles are interchanged in the wave function: $\Psi(\vec{r_i}, \bar{\sigma}_i, \vec{r_j}, \bar{\sigma}_j) = -\Psi(\vec{r_j}, \bar{\sigma}_j, \vec{r_i}, \bar{\sigma}_i)$. This is a direct consequence of Pauli's exclusion principle, which states that no two fermions can occupy the same quantum state. We will use Ψ for many-body wave functions and ψ for single-particle wave functions. The last part in Equation A.4 is the energy, the eigenvalue of Schrödinger's equation. The energy is an observable property, something one can (in principle) measure. It corresponds to the difference in energy of the many-body system in its ground state, and of all constituting particles, non-interacting, at infinite distance from each other.

We can already simplify the afore mentioned Hamiltonian by applying the Born-Oppenheimer approximation (also known as the adiabatic principle), in which we consider the nuclei as static or "frozen". This approximation is most often valid since the nuclei's mass is much larger than the electrons' mass. Protons and neutrons are more than 1800 times heavier than electrons. Consequently, at a given force, acceleration and hence, velocity, of the nuclei is extremely small compared to the electron velocity. On the one hand, this turns the nuclear degrees of freedom in the wave function from variables to parameters. On the other hand it removes the nuclear kinetic energy from the Hamiltonian and turns the Coulomb interaction between nuclei and nuclei into a constant so that it could just be added to the eigenvalue. Electrons move in an electrostatic potential resulting from a static collection of nuclei:

$$V_{ext} = \frac{1}{4\pi\epsilon_0} \sum_{i,A} \frac{-e^2 Z_A}{|\vec{r_i} - \vec{R_A}|}. \tag{A.6}$$

Since this potential is given for a certain system, it is often referred to as the external potential. The electron-nuclei interaction defines the system i.e. it defines what kind of molecule or solid is being studied.

Another important principle to discuss is the electron density, ρ. The electron density is an observable property, which is defined as the probability of finding an electron at a point in space,

for all points in space. For a one-electron system it can be expressed as the modulus squared of the wave function, $\rho(\vec{r}) = \Psi^*(\vec{r})\Psi(\vec{r}) = |\Psi(\vec{r})|^2$, where the asterisk denotes the complex conjugate of the wave function. Accordingly, $\rho(\vec{r}) = \sum_{i=1}^{N} |\psi(\vec{r_i})|^2$, for a N-electron system in which the many-body wave function, Ψ, can be written by one-electron wave functions, ψ. It can then be interpreted as the probability of finding any electron at a point in space, regardless of where the other electrons are. The electron density is also a function which maps three spatial degrees of freedom (neglecting spin) onto a probability value, $\mathbb{R}^3 \rightarrow \mathbb{R}$. It is obviously much simpler than the wave function.

Now that some important basics are covered, we can approach DFT. The cornerstone of the theory is the 1st theorem of Hohenberg and Kohn [80]. The relationship between the external potential and the wave function is bijective. This means that there is exactly one wave function for a given external potential and, vice versa, only one external potential can correspond to a certain wave function. Since the wave function contains everything one can know about a system and the external potential defines a system, this relationship is rather obvious. The relationship between the wave function and the electron density is maybe not that intuitive. There seems to be no clear reason why two different wave functions should not result in the same electron density. However, this bijection is exactly what the 1st Hohenberg-Kohn theorem states for a system in its ground state. It is proven *reductio ad absurdum*. Consequently, there is a bijective (one-to-one) correspondence between the external potential and the ground state electron density of a many-electron system. Therefore, any ground state property of such a system can be expressed as a unique functional (a functional is a function of a function) of the ground state electron density. As already mentioned, this reduces a N-electron problem from 3N spatial degrees of freedom to only the 3 spatial degrees of freedom of the electron density. Despite this mayor simplification of the problem, there is still one inconvenience: Although the theorem proofs that such a unique functional does exist, it does not state anything about what this functional may look like.

One can take the total energy, as it appears in the Schrödinger equation, as an observable ground state property. Since the nuclei-electron interaction is described by the external potential and the nuclei-nuclei interaction is a constant, the unknown Hohenberg-Kohn density functional would only describe the electrons' kinetic energy and their interaction with each other. Now the

2nd Hohenberg-Kohn theorem [80] states that the density functional, which outputs the ground state total energy, has its global minimum at the ground state electron density. In other words, applying this (still unknown but unique) functional to the ground state density will output the lowest possible energy. This theorem is quite useful from a practical perspective because it suggests that by minimizing the total energy, one can find the ground state electron density and thereby, everything one can know about the system.

Kohn and Sham [81] derived a mathematically exact expression for the ground state electron density of a N-electron system, in which it is written as the sum of products of uncoupled single-particle equations with their complex conjugates:

$$\rho(\vec{r}) = \sum_{i=1}^{N} \psi^*(\vec{r_i})\psi(\vec{r_i}). \tag{A.7}$$

These single-particle wave functions are the lowest-energy solution of the Kohn-Sham equations:

$$H_{KS}\psi_i = \epsilon_i \psi i. \tag{A.8}$$

They look very similar to the many-body Schrödinger equation; however, it should be noted that the single particles of the Kohn-Sham equations do not represent real electrons but rather a mathematical construction of quasi-particles. The corresponding Hamiltonian,

$$H_{KS} = -\frac{\hbar^2}{2m}\nabla^2 + V_{ext} + \frac{e^2}{4\pi\epsilon_0}\int \frac{\rho(\vec{r'})}{|\vec{r} - \vec{r'}|}d\vec{r'} + V_{xc}, \tag{A.9}$$

contains the now well-known kinetic energy and the external potential. It also contains a so called Hartree term, which is the Coulomb energy of the particle in the electrostatic potential generated by all other particles (i.e. by the corresponding electron density). Since interactions with the overall electron density are considered, the 1/2 term does not appear here. The last contribution is the exchange-correlation energy which itself contains the exchange-correlation functional, F_{xc}:

$$V_{xc} = \frac{\delta F_{xc}[\rho]}{\delta\rho}. \tag{A.10}$$

This is the afore mentioned unique but unknown density functional, which will soon be discussed in more detail. If it were known, the Kohn-Sham method could be used to calculate the exact ground state electron density. Compared to the many-body Schrödinger equation, the mathematics is a lot

easier to solve. The fact that the expression for the density in Equation A.7 contains the density itself in H_{KS}, already foreshadows that a self-consistent solution scheme will be needed, which will also be discussed a bit further below.

The real exchange-correlation functional is probably extremely complicated since it is able to describe any molecule or solid and there is little hope that it will ever be found. Hence, at this point a second approximation has to be made. The most straightforward one is the local density approximation (LDA) [80]. For a homogeneous electron gas (a.k.a. jellium) with a certain electron density, the exchange-correlation energy, ϵ_{xc}, can be obtained from existing corrections to the free-electron model. LDA integrates over infinitely small volume elements of a system and assumes the exchange-correlation energy for each element equals the one of a homogeneous electron gas which has the same electron density as the element:

$$V_{xc}^{LDA}[\rho(\vec{r})] = \int \rho(\vec{r})\epsilon_{xc}[\rho(\vec{r})]d\vec{r}. \tag{A.11}$$

This method, though simple, already delivers reasonable results for some material classes and is an ingredient of more advanced classes of functionals. One of those classes are the generalized gradient approximations (GGA, e.g. PW91 [82], PBE [54], BLYP [83, 84]), which do not only consider the local electron density, but also how it changes with respect to the neighbouring elements:

$$V_{xc}^{GGA}[\rho(\vec{r})] = \int \epsilon_{xc}[\rho(\vec{r})]\nabla\rho(\vec{r})d\vec{r}. \tag{A.12}$$

So far we did not mention what exchange and correlation actually are. Exchange is a purely quantum mechanical phenomenon that does not have a classical analogy, and it does not mean that electrons exchange something with other electrons. It stems from the before mentioned fact that wave functions of electrons are antisymmetric for exchanging the electrons (i.e. interchanging the spatial and spin coordinates) in the wave function. In a simplified way that means that there is a Coulomb-similar interaction where the single-electron wave functions overlap, which makes it additionally unfavourable for electrons to come close to occupying the same quantum state. This is also known as Pauli's repulsion. Correlation is just the difference in energy between independent two-body solutions and the exact solution where all bodies are correlated. One can draw a classical mechanics analogy to a solar system where the gravitational interaction of the sun and a planet is

additionally dependent on the gravitational influences of the other planets.

In principle we now have all the essentials to think about how to actually do a DFT calculation. By solving the Kohn-Sham equations one can get the ground state electron density and energy; but to do so, the single-particle wave functions have to be found first. There are methods to express arbitrary wave functions as a collection of known simple functions. A prominent example is describing a wave of a certain shape as a Fourier series with weighted sine and cosine terms. More generally, the single-particle wave functions, ψ_i, can be described exactly by an infinite basis set consisting of chosen basis functions, χ_α^i, weighted by coefficients that have to be determined:

$$\psi_i(\vec{r}) = \sum_{\alpha=1}^{\infty} c_\alpha^i \chi_\alpha^i(\vec{r}). \tag{A.13}$$

In practice, of course, the basis set cannot be infinite and one has to choose a reasonable truncation. A few popular choices of basis functions will be discussed later. The great advantage of using a basis set expansion is that it turns the search for the wave functions into an algebraic eigenvalue problem. Using the bra-ket notation (also known as Dirac's notation), the Kohn-Sham equations can be written as $H_{KS}|\psi_i\rangle = \epsilon_i|\psi_i\rangle$, and left-multiplied with a bra, $\langle\psi_i|$, so that $\langle\psi_i|H_{KS}|\psi_i\rangle - \epsilon_i\langle\psi_i|\psi_i\rangle = 0$. With the basis set expansion this becomes $\sum_\alpha(\langle\chi_\alpha^i|H_{KS}|\chi_\beta^i\rangle - \epsilon_i\langle\chi_\alpha^i|\chi_\beta^i\rangle)|c_\beta^i\rangle = 0$. Summarizing the Hamiltonian matrix and overlap matrix elements as $H_{\alpha\beta} = \langle\chi_\alpha^i|H_{KS}|\chi_\beta^i\rangle$ and $S_{\alpha\beta} = \langle\chi_\alpha^i|\chi_\beta^i\rangle$, respectively, the generalized eigenvalue problem $\sum_\alpha(H_{\alpha\beta} - \epsilon_i S_{\alpha\beta})c_\beta^i = 0$ can be solved by matrix diagonalisation. In practice this can be merged to one big matrix equation, containing all the single-particle Kohn-Sham equations. In fact, matrix diagonalisation is what takes most of the computational time.

When all the single-particle wave functions are found, one can obtain the ground state density. But the density is needed to construct the Hamiltonian, and the Hamiltonian is needed to find the single-particle wave functions. Basically, the solution has to be known before it is calculated. The way to deal with this problem is the iterative self-consistent field (SCF) scheme, visualized in Figure A.4. It starts with a guess for the electron density with which the effective potential is calculated. The Kohn-Sham equations are then solved in the way described above. From the single-particle wave functions, a new value for the density is constructed. If this value (or the total energy) is close enough to the input value, the field is converged and the problem is solved. If not, the new density
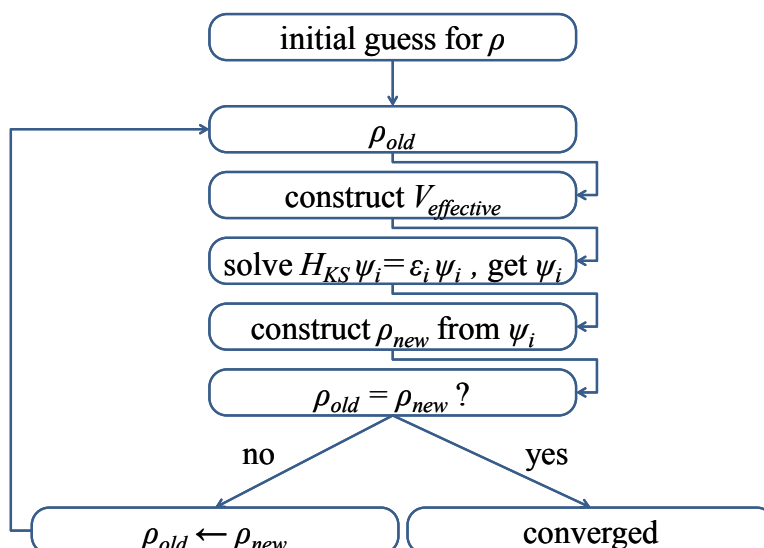
Figure A.4: *A schematic of the self-consistent field (SCF) method.*

value is used as input for the next SCF cycle, until the calculation converges.

We will now leave the very general path and look into some details. It has been discussed why it is useful to use a basis set expansion, but not yet how to construct a basis set. Since molecules and solids are made from atoms, an intuitive idea is to take atomic orbitals as basis functions. Atomic orbital basis sets are e.g. used in the OpenMX code [53]. If these functions are written in spherical coordinates, the angular parts of the functions are, possibly numerically optimized, spherical harmonics. So called spherical harmonics are functions that contain the l and m quantum numbers and define the shape of atomic orbitals. The radial parts of the basis functions will, in practice, be truncated at some cut-off radius. Advantages of this method are that it introduces some chemical insight in the calculation and allows using a relatively small basis set, which means fewer calculations are necessary. On the other hand, the math becomes more complicated because the basis functions are not orthogonal and therefore the overlap matrix S will not be diagonal. Furthermore, the basis sets depend on the atoms' positions and can (or cannot) overlap with each other, which can introduce some imprecision in dynamic problems due to varying basis set superposition.

Another popular, less localized, choice of basis functions are plane waves. To understand plane wave basis sets, one should be familiar with the concepts of reciprocal lattices, Brillouin zones, Bloch's theorem, and the behaviour of electrons in crystals, in general (see e.g. [67, 85, 86]).

Explaining these concepts in detail would go way beyond the scope of this text; therefore, it is assumed that they are known. According to Bloch's theorem, the wave function of a single electron in a crystal can be written as a plane wave multiplied with a function, $u_{\vec{k}}^n(\vec{r})$, which has the periodicity of the lattice (e.g. the periodic potential in which the electron moves):

$$\psi_{\vec{k}}^n(\vec{r}) = e^{i\vec{k}\vec{r}} u_{\vec{k}}^n(\vec{r}). \tag{A.14}$$

Here the wave vector $\vec{k}$ is a reciprocal space vector within the 1st irreducible Brillouin zone, and n is a band index which iterates over the higher reducible Brillouin zones. Furthermore, the reciprocal lattice can be described by a set of reciprocal lattice vectors, $\vec{G}$, which result in plane waves that are commensurate with the real lattice. This means that the function $u_{\vec{k}}^n(\vec{r})$, having the periodicity of the lattice, can also be written in a basis of plane waves with reciprocal lattice vectors. The electron density has the periodicity of the lattice, as well, and it was already stated that it corresponds to the modulus squared of the wave function. So, for an infinite periodic system, one has to sum up the moduli squared for all the bands n (here, without taking care of band occupation), integrated over all the $\vec{k}$ vectors in the 1st Brillouin zone (BZ), normalized by the volume, Ω_{BZ}, of the 1st Brillouin zone. In an infinite crystal, the $\vec{k}$ vectors are continuous, which is, of course, impossible to implement in a numerical calculation. In practice, the expression above is evaluated only for a finite number of points in the Brillouin zone, the so-called k-points. This procedure is comparable to a Riemann summation. If a very large system is simulated, it will be very small in reciprocal space and even a single k-point might be enough. This method of k-point sampling is not only used for plane waves, but for virtually any choice of basis functions, also for atomic orbitals.

Another procedure that makes the use of plane wave basis sets more affordable is the use of pseudo-potentials. Close to the nucleus, the real wave functions contain some very steep features, while they are smoother further away from the nucleus. Since the single-particle wave functions of the electrons have to be orthogonal, the core electrons would transfer steep features to the valance electrons. To accurately describe these steep features in a plane wave basis, one would need a very large basis set. However, the core electrons just screen the nuclear charge from the valence electrons, weakly dependent on the chemical environment, and do not take part in chemical bonding. By using a pseudo-potential, one considers nuclei and core electrons as an effective potential (i.e.

as "frozen") and replaces the valence electrons' wave functions by a smooth pseudo-wave function close to the nucleus, leaving it unchanged further away from the nucleus. Pseudo-potentials are usually generated by performing calculations on single atoms with all electrons. Plane waves with pseudo-potentials can e.g. be used in the Quantum Espresso [87] or VASP [55] code, even though in VASP this is seldom done. Obviously, it saves a lot of computational resources to not calculate the core electrons separately; therefore, this method is not only used with plane wave basis sets but everywhere where one is interested in the valence electrons only. In comparison to atomic orbital basis sets, plane waves are orthogonal and independent of the atomic position and species. They are often the natural choice for solid state problems due to their periodicity. On the downside, basis sets have to be relatively large to mimic atomic orbitals and the usage of pseudo-potentials is mandatory, which can introduce non-physical artefacts if the potential is inaccurate.

There is a third family of "augmented" wave basis sets that unites advantages of both the plane wave and atomic orbital approaches, which will be discussed only in brief. For a more thorough description of the underlying mathematics, refer to given references. Members of that group are e.g. augmented plane waves (APW) [88], linearized augmented plane waves (LAPW [89], used e.g. in the WIEN2k code [90] as LAPW+lo), and projector augmented waves (PAW [91], used e.g. as the most common method in the VASP code). In these methods, the system's volume is partitioned in spherical regions around the atoms (a.k.a. muffin tin spheres) and the space in between the atoms. For the APW method, the basis set consists of normal plane waves in the interstitial region, but of atomic orbital-like functions (angular spherical harmonics plus a radial part) within the spheres around the atoms. To make the transition continuous at the sphere boundaries, plane waves are expanded in Bessel functions around the centre of the sphere and the spherical harmonics coefficients are chosen to match them at the sphere boundaries. Using this description, the single-particle wave functions will unfortunately be energy-dependent, which means that it requires a lengthy iterative self-consistent procedure to determine them. The linearized APW (LAPW) method gets around this problem by Taylor-expanding the radial part of the atomic orbital-like functions and truncating the expansion after the linear term. The coefficients of this term contain the energy and can be determined by matching them with the value and slope of the function at the sphere boundary. Employing this

method with some further local orbital (+lo) [92] extensions in an all-electron calculation is known to produce extremely accurate results for a given exchange-correlation functional, and often serves as a comparison for other methods. In the PAW method, a single-particle wave function is expressed as a sum of three contributions which can all be described in a separate basis set: A smooth pseudo-wave function defined everywhere in a plane wave basis, a steep all-electron one-centre wave function inside the spheres in an atomic orbital-like basis, and subtracted from the previous ones, a smooth pseudo-one-centre wave function inside the spheres in an atomic orbital-like basis. A linear transformation transforms the pseudo-wave function to the all-electron one-centre wave function, which differs only inside the atom spheres. The coefficients of the pseudo-one-centre wave function inside the spheres can then be obtained from an inner product with so-called projector functions. The PAW method is usually also used with pseudo-potentials in which the core electrons are considered as "frozen". Within the frozen-core approximation, the PAW method is considered to combine, to some degree, the accuracy of LAPW with the computational efficiency of plane waves.

There are many more methods and approximations used within the broad realm of applied density functional theory that concern very different sections of the computational process; but going into more detail here would go beyond the scope of a quick introduction. Nevertheless, when performing actual calculations, it is essential to be aware of important technical details, to assure that the results are as accurate as possible.